The Astrophysical Journal, 887:200 (20pp), 2019 December 20 https://doi.org/10.3847/1538-4357/ab55e3

A Dissection of Spatially Resolved AGN Feedback across the Electromagnetic Spectrum

Travis Fischer[1,2,3], Krista Lynne Smith[4], Steve Kraemer[2], Henrique Schmitt[5], D. Michael Crenshaw[6], Michael Koss[7], Richard Mushotzky[8], Kirsten Larson[9], Vivian U[10], and Jane Rigby[3]
[1] U.S. Naval Observatory, 3450 Massachusetts Avenue NW, Washington, DC 20392, USA
[2] Institute for Astrophysics and Computational Sciences, Department of Physics, The Catholic University of America, Washington, DC 20064, USA
[3] Observational Cosmology Lab, Goddard Space Flight Center, Code 665, Greenbelt, MD 20771, USA
[4] KIPAC at SLAC, Stanford University, Menlo Park, CA 94025, USA
[5] Naval Research Laboratory, Washington, DC 20375, USA
[6] Department of Physics and Astronomy, Georgia State University, Astronomy Offices, 25 Park Place, Suite 600, Atlanta, GA 30303, USA
[7] Eureka Scientific, 2452 Delmer Street Suite 100, Oakland, CA 94602-3017, USA
[8] Department of Astronomy and Joint Space-Science Institute, University of Maryland, College Park, MD 20742, USA
[9] Infrared Processing and Analysis Center, MC 314-6, Caltech, 1200 E. California Blvd., Pasadena, CA 91125, USA
[10] Department of Physics and Astronomy, 4129 Frederick Reines Hall, University of California, Irvine, CA 92697, USA
Received 2019 August 19; revised 2019 October 21; accepted 2019 November 8; published 2019 December 19

Abstract

We present optical SuperNova Integral Field Spectrograph integral field spectroscopy, *Hubble Space Telescope* optical imaging, *Chandra* X-ray imaging, and Very Large Array radio interferometry of the merging galaxy 2MASX J04234080+0408017, which hosts a Seyfert 2 active galactic nucleus (AGN) at $z = 0.046$. Our observations reveal that radiatively driven, ionized gas outflows are successful to distances >10 kpc due to the low mass of the host system, encompassing the entirety of the observed optical emission. We also find that at large radii, where observed velocities cannot be reproduced by radiative driving models, high-velocity kinematics are likely due to mechanical driving from AGN winds impacting high-density host material. This impacting deposits sufficient energy to shock the host material, producing thermal X-ray emission and cosmic rays, which in turn promote the formation of in situ radio structure in a pseudo-jet morphology along the high-density lanes.

Unified Astronomy Thesaurus concepts: Extragalactic radio sources (508); AGN host galaxies (2017); Active galactic nuclei (16); X-ray active galactic nuclei (2035); Radial velocity (1332); Spectroscopy (1558); Galaxy kinematics (602)

1. Introduction

There is clear and demonstrable evidence for a relationship between supermassive black holes (SMBHs) and the physical properties of their host galaxies. Tight correlations exist between the black hole mass and the stellar bulge mass, bulge luminosity, and stellar velocity dispersion (Ferrarese & Merritt 2000; Gebhardt et al. 2000; Gültekin et al. 2009). The probable mechanism for such correlations is feedback from an active galactic nucleus (AGN) (Begelman 2004) on the host galaxy. The existence of an AGN could either quench star formation in the host galaxy by expelling or heating the necessary molecular gas (e.g., Di Matteo et al. 2005; Hopkins & Beacom 2006) or trigger star formation by instigating outflows that generate turbulence and shocks, causing the collapse of giant molecular clouds (Klamer et al. 2004). These effects may be one of the main drivers of evolution in massive galaxies: AGN feedback is necessary in cosmological simulations to suppress the formation of massive blue galaxies (Hopkins et al. 2008; Cattaneo et al. 2009). Further, AGN host galaxies tend to lie in the otherwise sparsely populated region between the blue, star-forming sequence and red ellipticals on color–mass plots (Nandra et al. 2007; Schawinski et al. 2009; Koss et al. 2011), and appear to have suppressed star formation rates for a given total stellar mass compared to normal galaxies (Salim et al. 2007; Shimizu et al. 2015; Ellison et al. 2016). However, the observed correlations between the black hole and the host galaxy could also be a result of co-evolution, in which galaxy mergers instigate both the fueling of the black hole and star formation.

Many surveys have made progress in understanding the effects of feedback on galaxy evolution writ large (e.g., Müller-Sánchez et al. 2018; Riffel et al. 2018; Neumann et al. 2019). An important complement to this approach is studying the detailed interaction of an AGN and its host galaxy in individual objects. Recently, we analyzed kinematics in the luminous, nearby ($z = 0.017$) Seyfert 2 galaxy Mrk 573 (Fischer et al. 2017), where we found the AGN-ionized gas morphology to be consistent with an intersection between spiral arms in the host disk and ionizing radiation from the central engine. Dust lanes rotating in the host disk, traced by molecular hydrogen emission, were found to connect regions of ionized gas from outside the biconical AGN radiation field, suggesting that kinematics of the outflowing ionized gas in the narrow-line region (NLR) of Mrk 573 are due to in situ acceleration of material originating in the host disk via radiative driving by the AGN, until radiative driving is no longer able to disrupt the rotational motion of the spiral arms, forming the extended NLR (ENLR).

Another individual galaxy potentially capable of providing similar insights is 2MASX J04234080+0408017, henceforth 2MASX J0423, shown in Figure 1. A merging system that houses a Type 2 AGN, 2MASX J0423 exhibits bright optical ionized gas extents on scales of several kiloparsecs, and potentially provides an excellent opportunity to measure high-resolution ionized gas outflows to much larger distances.

Alongside extensive optical ionized gas structures, the object has large radio lobes that extend well outside the host galaxy, spanning approximately 30 kpc, as first reported by Beichman et al. (1985). At the time, the host was thought to be a spiral

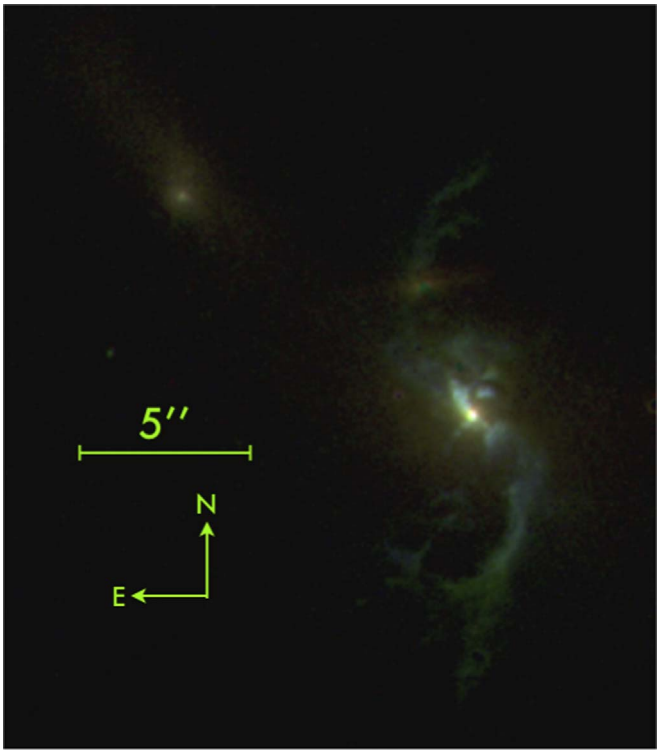

Figure 1. *Hubble Space Telescope* imaging of the merging AGN 2MASX J0423 (right) with companion (left). A third, background galaxy at a different redshift is in the northern limb of 2MASX J0423 at approximately 4.″1 from the continuum peak. Color rendition is composed of *HST*/WFPC2 F814W (red), F675W (green), and F547M (blue) filters. 5″ corresponds to a spatial scale of ∼4.5 kpc.

galaxy. However, optical spectroscopy by Hill et al. (1988) found that the spiral structure was not produced by starlight or scattered nuclear light. Steffen et al. (1996) analyzed the kinematics in more detail and found the radio structure to be bent along the optical ionized spiral. Using long-slit spectroscopy of the radio lobes, Holloway et al. (1996) found that the radio lobes have optical emission lines with velocity differentials of $\sim$1000 km s^{-1}, and suggested that the radio jet expands dramatically into the observed lobes after emerging from the dense interstellar medium.

After this, the galaxy remained unstudied for many years before having the good fortune to be detected as part of the ultrahard X-ray-selected *Swift*-BAT AGN sample, which has been the subject of a large multi-wavelength follow-up effort (Koss et al. 2017). A 22 GHz high-resolution radio imaging survey of the BAT AGN (Smith et al. 2016) obtained a much more sensitive radio image of 2MASX J0423 than those previously available. A *Chandra* survey of merging galaxies (Koss et al. 2012) included this system, although only a single AGN was detected, with complementary optical spectroscopy to also identify dual AGNs using SuperNova Integral Field Spectrograph (SNIFS) integral field unit (IFU) observations. The new data present an opportunity to learn more about the AGN/host galaxy interaction in this unique object. In this paper, we synthesize all of these observations and use them to scrutinize the conclusions of the work in the 1980s and 1990s and add our own insights.

In our analysis of 2MASX J0423, we use a redshift of $z = 0.046099$ (Springob et al. 2005), a Hubble constant of $H_0 = 71$ km s^{-1} Mpc^{-1}, $\Omega_m = 0.3$, and $\Omega_\lambda = 0.7$ for a Hubble distance of 201.5 Mpc and a scale of 0.893 kpc arcsec^{-1} (Wright 2006).

2. Observations and Reduction

2.1. Hubble Space Telescope (HST) Imaging Observations

Archival *HST* Wide Field and Planetary Camera 2 (WFPC2) imaging was retrieved from the Mikulski Archive at the Space Telescope Science Institute. The observations were obtained on 1995 January 31 as a part of Program ID 5746 (PI: F. D. Macchetto) with a plate scale of 0.″05 pixel^{-1}. Two exposures of 300 s each were taken using the F547M filter and individual 600 s exposures were taken using F675W and F814W filters. Cosmic rays were removed from the latter images using the L.A. Cosmic algorithm (van Dokkum 2001). F547M and F814W filters cover largely featureless continuum, while the F675W bandwidth covers [O I] λ6300, [N II] $\lambda\lambda$6548, 6584, Hα, and [S II] $\lambda\lambda$6716, 6731 emission lines.

2.2. UH 2.2 m/SNIFS Optical IFU Observations

Spectroscopic observations of 2MASX J0423 were obtained using SNIFS (Aldering et al. 2002; Lantz et al. 2004), mounted at the University of Hawaii 2.2 m telescope (UH88) at Maunakea on UT 2012 November 11 for a total of 7 hr of integration with an effective seeing FWHM for science observations of 0.″97 across three fields of view. The top left portion of Figure 2 depicts the positions of the SNIFS fields overlaid on a cropped F675W *HST* image. The center and bottom fields overlap by 2″, while the top field is offset from the center field by approximately 0.″4. Individual Hα flux distributions in the top, center, and bottom SNIFS fields illustrate the correspondence between morphologies observed in our SNIFS and *HST* observations.

SNIFS employs a fully filled 15 × 15 lenslet array in the IFU, covering a 6.″4 × 6.″4 field of view. The corresponding spatial resolution is 0.43 arcseconds per spatial pixel (spaxel). The spectrograph consists of two arms operating simultaneously to cover the entire optical wavelength range at $R \sim 1000$: the blue channel covers 3000–5200 Å and the red channel covers 5200–9500 Å. The SNIFS reduction pipeline, SNURP, was used for wavelength calibration, spectro-spatial flat-fielding, cosmic ray removal, and flux calibration (Bacon et al. 2001; Aldering et al. 2006). A sky image was taken after each source image and subtracted from each IFU observation. The extraction aperture was 2.″4 in diameter.

2.3. Chandra and NuSTAR X-Ray Observations

On 2012 October 20, 2MASX J0423 was imaged with the ACIS-S detector on *Chandra* for 20 ks. We reprocessed the image using the *Chandra* Interactive Analysis of Observations (CIAO) software version 4.11 (Fruscione et al. 2006). After restricting the energy to 0.3–7 keV with the task `dmcopy` to avoid the sharply rising high-energy particle background outside this range, we normalize by the exposure map and correct for bad pixels using the task `fluximage`.

In 2012 July, 2MASX J0423 was observed three times by *NuSTAR* as part of the BAT legacy survey. Each observation is approximately 6 ks in duration. Although the signal-to-noise ratio (S/N) is not sufficiently high for imaging, the hard energy range of *NuSTAR* ($\leqslant$78 keV) allows us to constrain the power-law component of the spectral fits from *Chandra*.

2.4. VLA Radio Interferometry Observations

On 2013 June 15, 2MASX J0423 was imaged by the Karl G. Jansky Very Large Array (VLA) in C-configuration. Observations were obtained in the *K*-band, centered at 22 GHz with an 8 GHz bandwidth, resulting in 1″ spatial resolution (Smith et al. 2016). The science integration for 2MASX J0423 was 7 minutes in duration and was preceded and followed by a pointing and gain calibration scan of the reference quasar J0433 +0521; the 1σ sensitivity in the science image is 20 μJy per beam. The entire observing block was concluded with a flux and bandpass calibration scan of 3C 48.

After collection, the raw data were passed through the standard VLA reduction pipeline at the National Radio Astronomy Observatory (NRAO). We then processed the data using the Common Astronomy Software Applications package (v. 4.5, CASA; McMullin et al. 2007). The calibrated science observation was split from the parent measurement set, averaging over all 64 channels within each spectral window in order to reduce processing time without compromising image quality. Finally, the image was cleaned to a 0.03 mJy threshold using the CASA clean task with Briggs weighting.

We also include archival images of 2MASX J0423 in the NRAO VLA Archive Survey (NVAS)[11] at 1.45 GHz and 4.89 GHz, taken in A-Configuration in 1995 September, which have similar resolutions to our 22 GHz image of 1.″33 and 0.″39, respectively.

3. Observational Analysis

3.1. SNIFS Spectroscopic Fitting

Emission-line kinematics and fluxes of [O II] λ3727, [Ne III] λ3869, Hβ, [O III] λ5007, [O I] λ6300, Hα, [N II] $\lambda\lambda$6548, 6584, [S II] $\lambda\lambda$6716, 6731, and [S III] λ9071 were measured in each spaxel of our SNIFS data cubes by fitting Gaussians in an automated routine, with example fits to spectra shown in Figure 2. Our fitting process, previously discussed in depth in Fischer et al. (2017), uses the Importance Nested Sampling algorithm as implemented in the MultiNest library (Feroz & Hobson 2008; Feroz et al. 2009, 2013; Buchner et al. 2014) to compute the logarithm of the evidence, ln *Z*, for models containing a continuum plus zero to two Gaussian components per emission line. When comparing two models, i.e., a model with zero Gaussians (M_0) and a model with one Gaussian (M_1), the simpler model is chosen unless the more complex model, M_1, has a significantly better evidence value, $|\ln(Z_1/Z_0)| > 5$ (99% more likely).

Several models were used to fit emission lines in each spaxel. [O III] models measured [O III] λ5007 and simultaneously fit a second set of components to [O III] λ4959 in order to properly account for possible flux contributions from wing emission between the two lines. Gaussian wavelength centroid and width parameters of [O III] λ4959 were fixed following parameters used in fitting [O III] λ5007, with the flux of [O III] λ4959 fixed to be one-third of the [O III] λ5007 flux. Hα + [N II] models fit Hα and [N II] $\lambda\lambda$6548, 6584 simultaneously. Gaussian wavelength centroid and width parameters of [N II] $\lambda\lambda$6548, 6584 were fixed following parameters used in fitting Hα, under the assumption that the lines originate from the same emission region, with the flux of [N II] λ6548 fixed to be one-third of the [N II] λ6584 flux, which was left as an open parameter. [S II] models fit [S II] $\lambda\lambda$6716, 6731 simultaneously, with Gaussian width fixed to be identical between lines. [O II] λ3727, [Ne III] λ3869, Hβ, [O I] λ6300, and [S III] λ9071 lines were fit individually.

Initial input parameters in our models are selected based on physical considerations. The centroid position for each Gaussian was limited to a 40 Å range around the wavelength that contained the entirety of the line profiles throughout each data cube. Gaussian standard deviation ranged from the spectral resolution of the blue and red gratings to an artificial FWHM limit of $\sim$1600 km s^{-1}. Gaussian height was defined to allow for an integrated flux that ranged from a 3σ detection to a maximum integrated flux of $3\sigma \times 10^4$.

Fit parameters for measured lines were used to calculate their observed velocity, FWHM, and integrated flux, mapped for [O II] λ3727, [O III] λ5007, and Hα in Figures 3–5, with additional measurements for [O I] λ6300, [S II] λ6716, [Ne III] λ3869, Hβ, and [S III] λ9071 lines for the nuclear field of view in the Appendix. The Doppler-shifted velocity for each emission-line component is given in the rest frame of the galaxy using air rest wavelengths of each line. We found emission lines present in most spaxels to be best fit with a single Gaussian.

Individual spaxel fits for Hβ were largely unsuccessful because the emission line was located near the edge of the detector in the blue data cubes. Therefore, we instead estimate observed Hβ fluxes from Hα observations by measuring the intrinsic reddening in each SNIFS field of view. We bin the blue and red cubes from each field of view into single spectra and compare the resultant Hβ and Hα flux peaks, assuming that the FWHMs across the two lines are identical, to measure Hα/Hβ ratios for the north, central, and south fields of 3.18, 4.02, and 4.64, respectively. We used these ratios along with the observed Hα flux maps to estimate Hβ fluxes across the system.

3.2. Optical Morphology

From the *HST* F547M/F675W/F814W imaging shown in Figure 1, the optical morphology of 2MASX J0423 is largely confined to an S-shape provided by two gas lanes north and south of the nucleus. The brightest structure is contained inside a radial distance of 1.″2 ($\sim$1 kpc) from the nucleus, observed in all three bands extending along the inner portion of the gas lanes. A background galaxy resides 4″ ($\sim$3.6 kpc) from the nucleus along the northern lane gas lane, visible in F675W/F814W imaging and absent in F547M imaging. Gas lanes extend north and south of the nucleus to approximately 7.″75 ($\sim$7 kpc) and the merger companion is located at a projected distance of approximately 10.″65 ($\sim$9.5 kpc) from the nucleus of 2MASX J0423.

It is unclear whether the observed lanes are loose spiral arms in the galaxy, because they are largely absent in the near-IR F814W imaging, suggesting little to no contribution from stellar emission (Hill et al. 1988), or filaments carved from the host disk by some form of AGN feedback. The host may also be morphologically disturbed due to the interaction with the nearby companion galaxy to the northeast as shown in Figure 1. The F814W imaging also suggests that a stellar stream connects the two galaxies, implying that at least one merger pass has occurred.

[11] http://archive.nrao.edu/nvas/

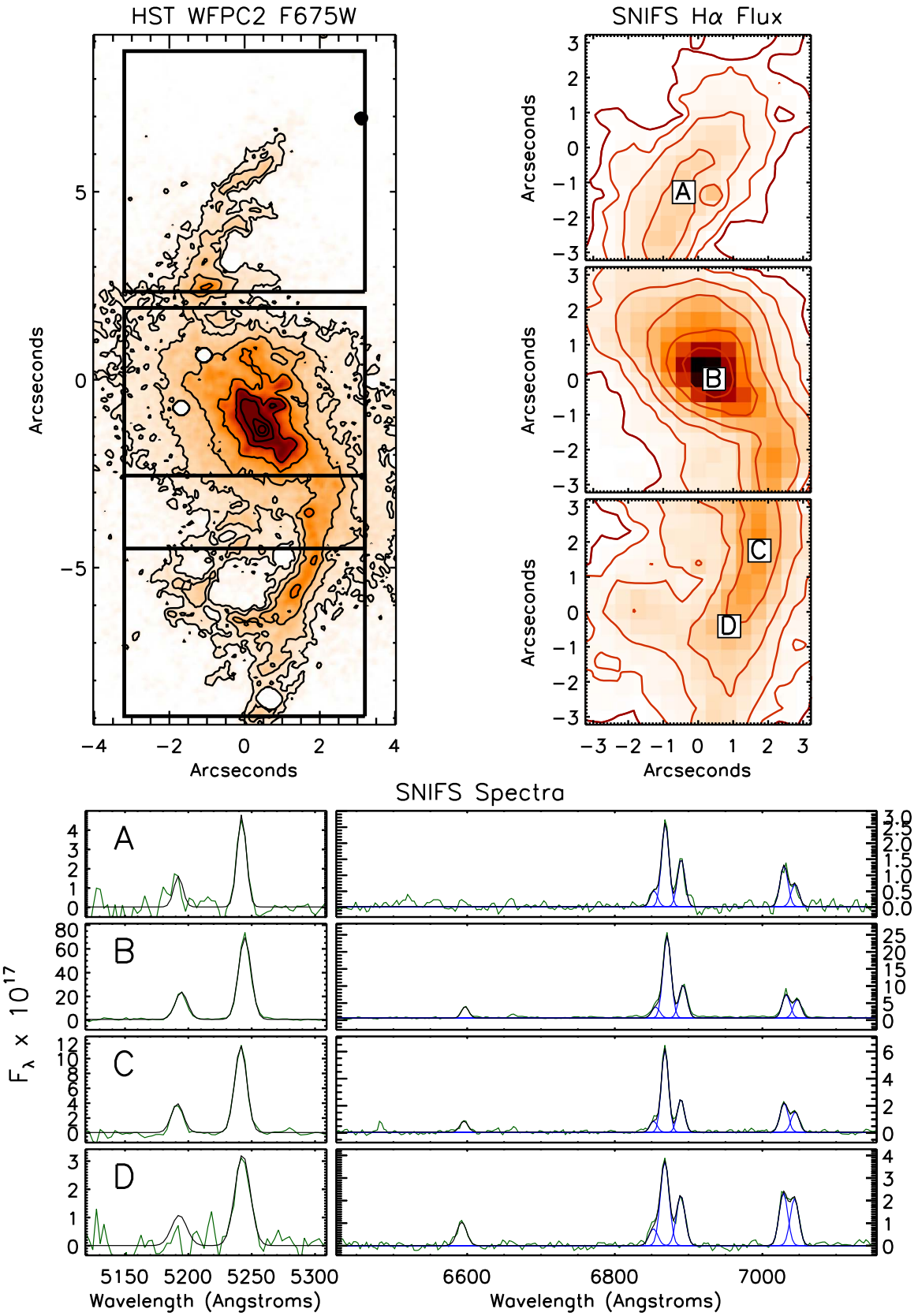

Figure 2. Top left: black squares depict the distribution of $6\farcs4 \times 6\farcs4$ SNIFS fields of view of 2MASX J0423 overlaid on an *HST*/WFPC2 F675W image. The top, center, and bottom fields are unevenly distributed, with the top field offset from the center field by approximately $0\farcs4$ and the center and bottom fields overlapping by approximately $2''$. White circles in the center SNIFS field box are artifacts. Top right: continuum-subtracted Hα flux distributions obtained from the top, center, and bottom $6\farcs4 \times 6\farcs4$ SNIFS data cubes. Outer, dark red contours represent a 3σ S/N lower flux limit. Bottom: representative spectra across 2MASX J0423, overplotted with their best fitting model. Approximate spaxel positions are labeled in the Hα image. Left boxes exhibit [O III] $\lambda\lambda$4959, 5007, right boxes exhibit [O I] λ6300 (when present), Hα + [N II] $\lambda\lambda$6549, 6585, and [S II] $\lambda\lambda$6718, 6732. Green represents data, blue represents individual Gaussians in blended emission lines, and black represents the combined model. The optical continuum flux peak of 2MASX J0423 is sampled in spectrum B. North is up and east is left in all images.

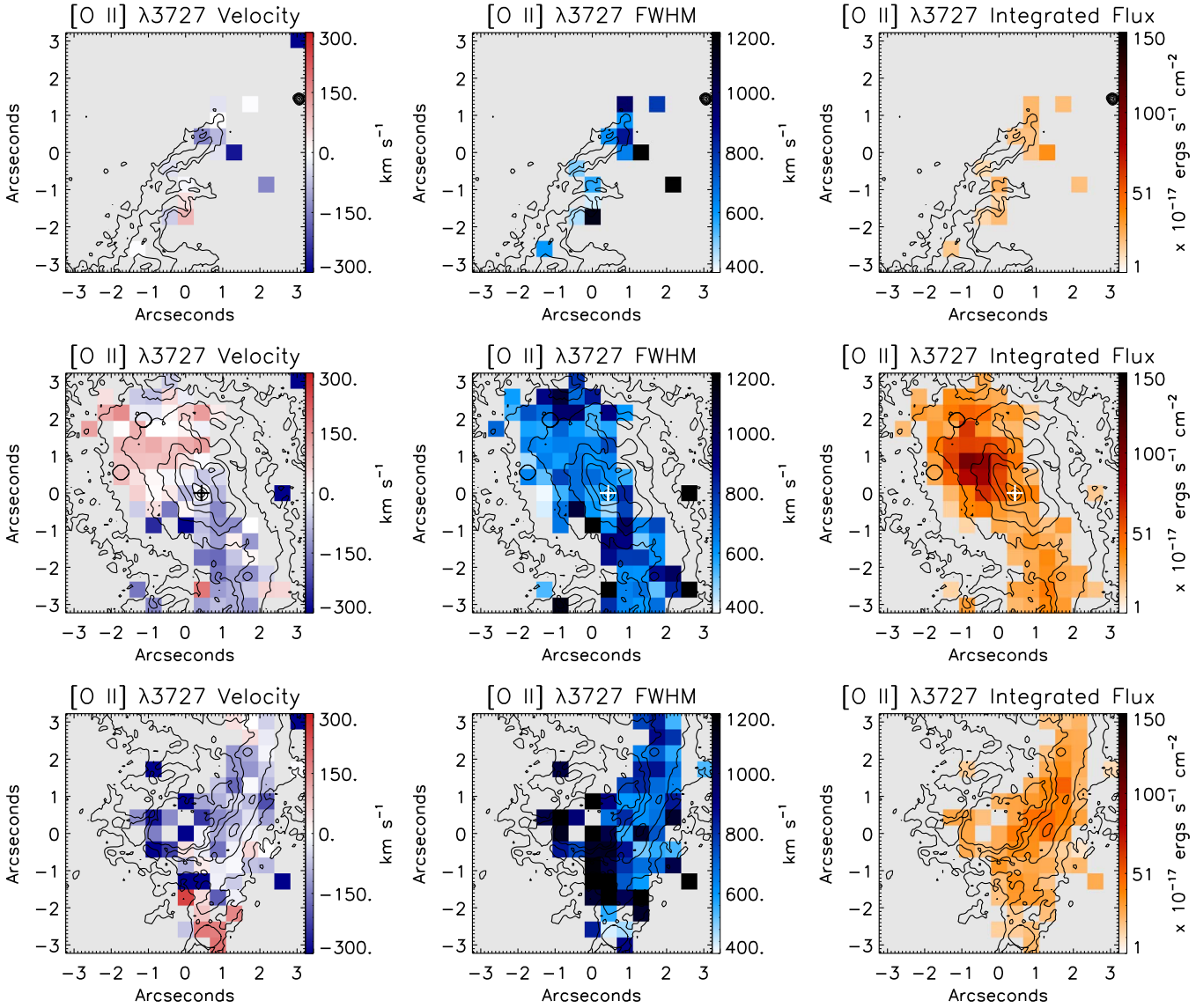

Figure 3. [O II] λ3727 kinematic measurements in 2MASX J0423 from SNIFS IFU observations. First, second, and third columns display emission-line profile centroid velocity, FWHM, and integrated flux maps, respectively. First, second, and third rows display measurements for the top, center, and bottom fields of view, respectively. Black contours represent *HST*/WFPC2 F675W imaging. The optical continuum flux peak is depicted by a cross. One $0\farcs4 \times 0\farcs43$ spaxel samples approximately 380 pc $\times$ 380 pc.

3.3. Ionization Source Diagnostics

We compare measured line flux ratios via three ionization diagnostic diagrams (i.e., BPT diagrams; Baldwin et al. 1981) to spatially resolve the source of ionization throughout the system. Figure 6 shows [O III]/Hβ versus [N II]/Hα, [S II]/Hα, and [O I]/Hα as a function of distance from the peak of the nuclear optical continuum for each of the three fields of view. We find most of the gas to be AGN-ionized across all three fields of view, with [S II] and [O I] diagnostics suggesting that a large portion of the southernmost regions and a few regions in the north lane exhibit LINER-like ionization. We can see that the 2D distribution of ionization sources, as shown in Figure 7, shows LINER-like emission in the south to be distinctly located near the end of the southern gas lane below $x \approx -0\farcs2$.

3.4. Optical Ionized Gas Kinematics

We overlay the *HST* F675W flux map onto the independently measured SNIFS kinematics of each emission line, by aligning the flux peak in the central cube with that observed in imaging, to provide high-resolution structural reference to our kinematics.

The central field of view is largely redshifted north of the nucleus, with bright flux profiles corresponding to the bright structures observed in imaging likely due to adjacent molecular gas lanes being ionized by the AGN (Fischer et al. 2017). South of the nucleus is a low-flux region that exhibits blueshifted velocities, adjacent to a bright gas lane that exhibits generally systemic velocities over the brightest regions, blueshifts on the concave side, and redshifts on the convex side. Velocities for more ionized line species are generally redshifted from emission lines of lower ionization potential across the field. FWHM measurements are lower along the bright structure in the field, and are higher in fainter regions directly north and south of the nucleus.

The bottom field of view follows the remainder of the south gas lane. Kinematics near the gas lane continue to exhibit blueshifts on the concave side and redshifts on the convex side,

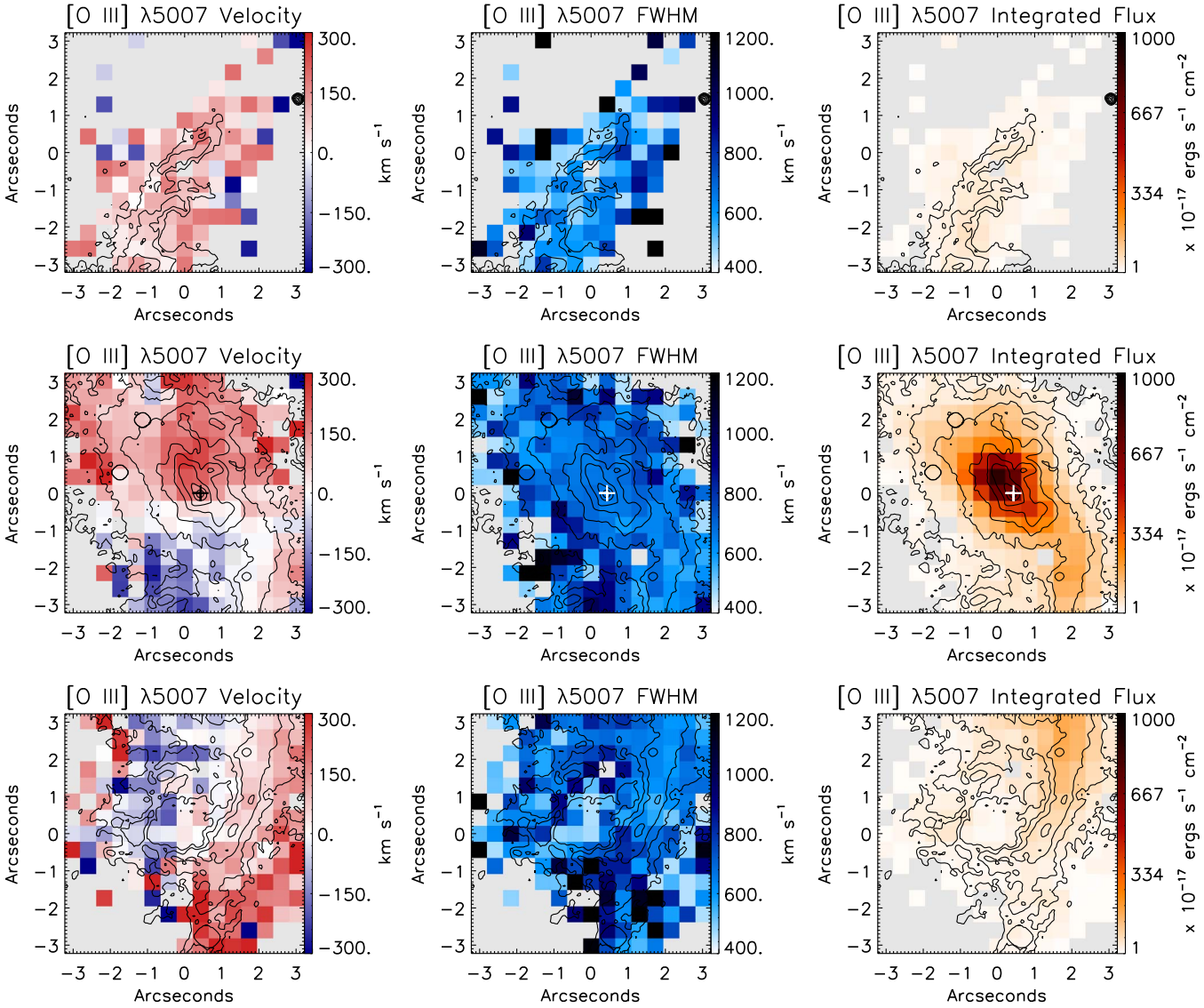

Figure 4. [O III] λ5007 kinematic measurements in 2MASX J0423 from SNIFS IFU observations. First, second, and third columns display emission-line profile centroid velocity, FWHM, and integrated flux maps, respectively. First, second, and third rows display measurements for the top, center, and bottom fields of view, respectively. Black contours represent *HST*/WFPC2 F675W imaging. The optical continuum flux peak is depicted by a cross. One $0\farcs4 \times 0\farcs43$ spaxel samples approximately 380 pc × 380 pc.

except for [O II] kinematics, which are largely blueshifted along the lane. Again, velocities of more ionized line species are generally redshifted in comparison to emission lines of lower ionization potential across the field. The largest velocity amplitudes across all emission lines are observed at the end of the lane, with peak blueshifts and redshifts corresponding to left and right splits of the gas lane morphology at the bottom of the field. The largest FWHM measurements in the system are also located at the splitting point in the south gas lane, reaching values greater than 1000 km s^{-1} with velocity offsets near systemic. The peaks in both velocity offset and FWHM reside the region predominantly exhibiting LINER-like emission in the bottom half of the southern field.

The top field of view traces the north gas lane. Flux distributions, offset velocities, and FWHMs in this field are similar to but generally of smaller amplitude than what is observed in the southern lane. Kinematics of the lane are generally redshifted, with evidence of blueshifts on the concave side of the lane in lower ionization states. The tip of the lane also exhibits an increase in FWHM, similar to the southern lane. This field also partly contains the background field galaxy along the north lane observed in Figure 1, but no corresponding spectral signatures are detected.

3.5. X-Ray Analysis

From the available *Chandra* observations, we produced images in three separate bands: soft (0.5–1.2 keV), medium (1.2–3 keV), and hard (3.0–7.0 keV), shown in Figure 8. We find the hard X-ray emission to be largely concentrated in the nucleus, while softer X-ray emission (0.5–3.0 keV) is extended, with 3σ detections largely extending to $\sim 12\farcs6$ (11.3 kpc) and one extended cloud to the northwest at $\sim 16\farcs7$ (15.0 kpc).

From the full-spectrum event file we extracted spectra using the task `specextract`. Nuclear and off-nuclear X-ray spectral fitting was performed of the two regions shown in Figure 8, with extracted spectra and the resultant fits with

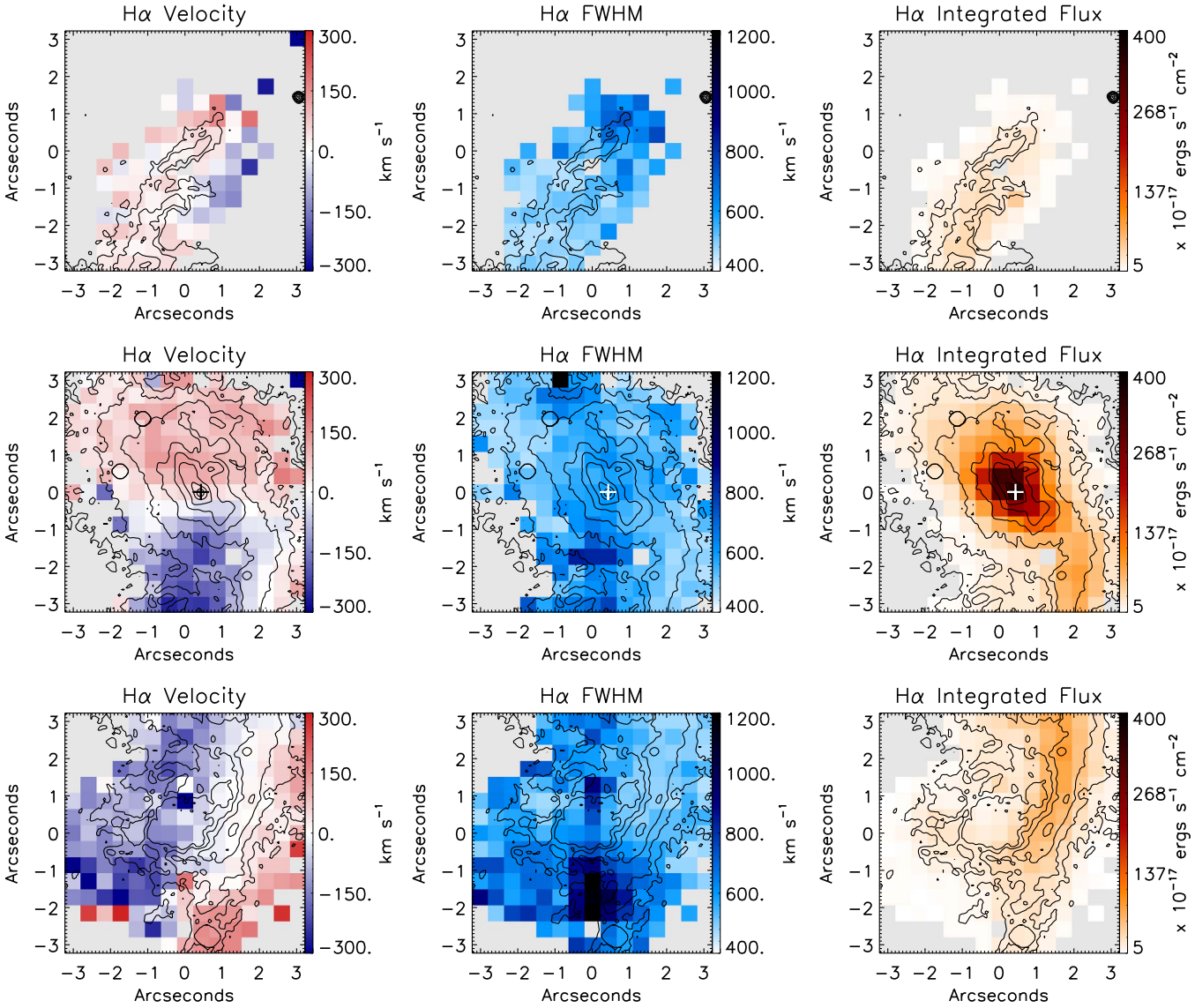

Figure 5. Hα kinematic measurements in 2MASX J0423 from SNIFS IFU observations. First, second, and third columns display emission-line profile centroid velocity, FWHM, and integrated flux maps, respectively. First, second, and third rows display measurements for the top, center, and bottom fields of view, respectively. Black contours represent *HST*/WFPC2 F675W imaging. The optical continuum flux peak is depicted by a cross. One $0\farcs4 \times 0\farcs43$ spaxel samples approximately 380 pc × 380 pc.

residuals shown in Figure 9. The nuclear spectrum is consistent with most Type 2 AGNs (Turner et al. 1997). It is well fit by a soft thermal component at $kT = 0.26 \pm 0.04$ keV with an abundance fixed at solar, an absorbed power law with a high column density (4.9×10^{23} cm^{-2}) and covering fraction (0.98), and a significant Fe Kα line at 6.4 keV in the rest frame. Combining the *Chandra* and *NuSTAR* spectra, we derive a power-law spectral index of $\Gamma = 1.45^{0.15}_{-0.16}$.

The X-ray spectrum of the southern X-ray lobe is best fit by a soft thermal plasma model with $kT = 0.97^{+0.106}_{-0.133}$ keV with an abundance fixed at solar. However, the signal-to-noise ratio is not sufficient to differentiate significantly between photoionized, shocked, and collisional equilibrium plasmas. Similar analysis of the northern lobe is not possible due to its relative faintness, because the spectrum from the northern lobe has too few data points to constrain the fitting parameters. However, the observed emission is consistent with the thermal properties of the southern lobe.

Comparing the X-ray emission with *HST* imaging, as shown in Figure 10, the X-ray morphology follows a similar extended morphology to what is observed in the optical. X-ray flux peaks outside the nuclear region are located near the ends of the observed optical gas lanes and coincident with the pockets of high FWHM emission exhibited in our SNIFS IFU observations. Neither the merger companion nor the background galaxy in this system appears to have a corresponding X-ray signature.

3.6. Radio Analysis

Radio morphologies via VLA observations across 1.45, 4.89, and 22 GHz bands are shown in Figure 11, and are largely divided into three regions: a nuclear component and two extended lobe-like components north and south of the nucleus. The nuclear component can be resolved into two knots of emission in the 4.89 GHz observations, and is otherwise a single elliptical knot. The southern lobe is brightest directly

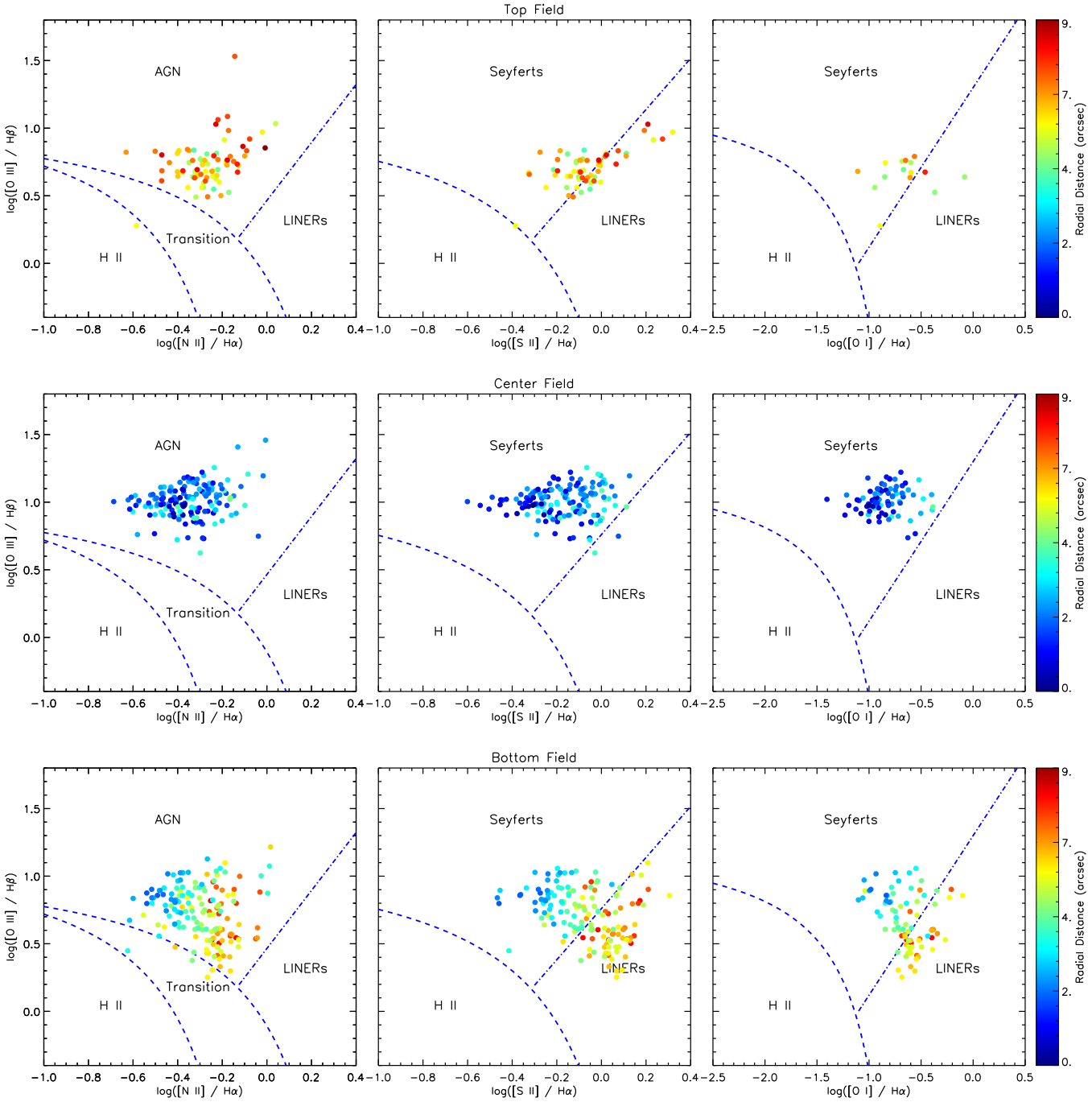

Figure 6. Ionization source diagnostics across 2MASX J0423 from SNIFS IFU observations. First, second, and third rows display diagnostics for the top, center, and bottom fields of view, respectively. Distances are projected and measured from the peak of the nuclear optical continuum in the central field of view.

south of the nuclear component and extends to the southeast in a fan shape primarily consisting of two elongated knots forking from the brightest knot. 4.89 and 22 GHz observations show that the brightest knot in the southern lobe is also composed of two elongated knots parallel with the knots at larger radii. The northern lobe is only observed in 1.4 and 22 GHz observations, is brightest directly north of the nuclear component, and extends northeast. The two bright knots in the northern lobe are connected by fainter emission and surrounded by a bubble with enhanced structure around the edges, particularly to the north of the brightest knots.

The spectral index α, where the flux density $S_\nu \propto \nu^\alpha$, of a radio source is often a useful diagnostic of the nature of the emission. Flat spectral indices ($-0.5 \leqslant \alpha \leqslant 0$) typically indicate extended thermal sources, while steep indices ($\alpha \leqslant -0.7$) indicate non-thermal synchrotron radiation; a compact non-thermal source that is optically thick will also result in a flat spectral index (Peterson 1997).

In order to create a spatially resolved map of spectral index, we have reprojected the archival 1.45 GHz image and our 22 GHz image using the Astropy package `reproject`. After measuring the mean rms noise in the background of both the 1.45 and 22 GHz images, we calculate the slope α between the 1.45 and 22 GHz flux densities at every pixel where both images have significant emission detected at $\geqslant 3\sigma$. The resulting spectral index map is shown in Figure 12, indicating

that bright, extended regions are due to non-thermal synchrotron radiation, discussed further in Section 5, with emission in the surrounding edges of the northern lobe originating from thermal sources such as shock heating. The nuclear knot exhibits a gradient in indices, with the southern portion that is closest to the optical and X-ray nucleus exhibiting a relatively flat index and the northern portion exhibiting a steep index. Again, compact emission near the nucleus can have a flat index because it is optically thick or because multiple synchotron-emitting regions are contained within the source, which we suggest is likely occurring here.[12]

We compare the morphologies and locations of the optical, X-ray, and radio emission in Figure 13. Immediately, we observe that the nuclear radio source is not centered on the optical and X-ray nucleus. The emission is instead located to the north in the region where we see bright optical structures and outflows adjacent to the nucleus. South of the nucleus, radio emission in the brightest knot is split into two elongated regions that straddle the optical gas lane before extending along the path of the gas lane arc to the southeast. X-ray and radio emission also follows the optical structure to the north, with X-ray emission located radially interior to adjacent radio structures. Assuming that the nuclear and southern straddled knots are adjacent to nuclear X-ray emission, X-ray emission being radially interior to adjacent radio structures is then prevalent throughout the system, likely structured by the location of molecular gas lanes highlighted by the observed optical emission.

4. Interpretive Analysis: Optical Kinematics

4.1. Rotation Kinematics

Observations that may provide spatially resolved stellar kinematics, and thus determine where the observed ionized gas kinematics are affiliated with rotation, are unavailable. As such, we use the observed [O II] kinematics in the central SNIFS field as a proxy, because large-scale [O II] emitting gas is less likely to be directly interacting with ionizing radiation from the AGN. However, [O II] in the north and south SNIFS fields is likely enhanced from other processes described below and is not included in this kinematic analysis. [O II] structure in the center SNIFS field is aligned with the gas lane structure observed in optical imaging, and the observed kinematics suggest that the north gas lane is redshifted, rotating into the plane of the sky, and the south gas lane is blueshifted, rotating out of the plane of the sky.

4.2. Radiatively Driven Kinematics

Comparing rotation kinematics to the velocities observed in [O III] and Hα emitting gas, as shown in Figure 14, we find a clear offset between the likely rotating gas and gas influenced by the AGN. In particular, large offsets in [O III] and Hα velocities are most visible immediately north of the nucleus. In order to determine whether radiative driving can produce the observed offsets in optical ionized gas velocity, we compare the gravitational deceleration to the radiative acceleration experienced by the gas within the inner 10 kpc of the system.

Using a method similar to the one used by Fischer et al. (2017) for Mrk 573, *HST* WFPC2/PC F814W imaging of

[12] Images are disparate in time by about 20 yr, although on this timescale only the unresolved radio core emission would vary.

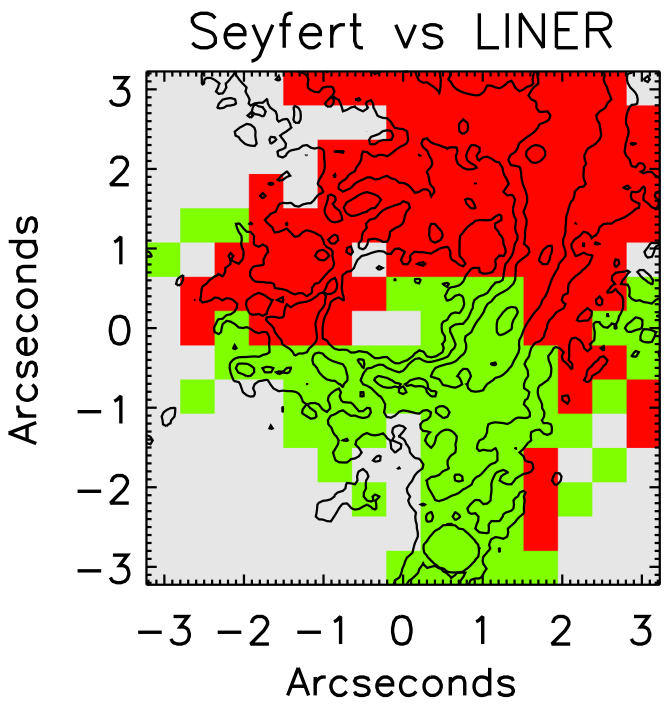

Figure 7. 2D distribution of the [O III]/Hβ vs. [S II]/Hα ionization source diagnostic for the south SNIFS field of view of 2MASX J0423 shown in Figure 6 with *HST*/WFPC2 F675W imaging contours. AGN- and LINER-dominated ionization sources are represented by red and green, respectively.

2MASX J0423 was decomposed using GALFIT version 3.0.5 (Peng et al. 2002, 2010) in order to measure enclosed mass and calculate gravitational deceleration in the galaxy as a function of radius. We find that the best fitting model is composed of three Sérsic components with parameters described in Table 1. The original image, GALFIT model, and resulting residual map are presented in Figure 15. Component 1 can be identified as a bulge that is aligned with the spiral arm structure. Component 2 is disk-like and elongated in the direction of the merger companion, possibly due to merger processes. Component 3 is the background galaxy north of the nucleus visible in Figure 1.

The radial mass distribution of these three components, shown in Figure 16, was calculated using the expressions from Terzić & Graham (2005). The Sérsic profile is given by the following expression (Peng et al. 2010):

$$\Sigma(r) = \Sigma_e \exp\left[-\kappa\left(\left(\frac{r}{r_e}\right)^{1/n} - 1\right)\right] \quad (1)$$

where $\Sigma(r)$ is the surface brightness, Σ_e is the surface brightness at the effective radius, κ is a constant that depends on n, the index of the Sérsic profile, and r_e is the effective radius.

The value Σ_e is calculated using the equation

$$F_{\rm tot} = 2\pi r_e^2 \Sigma_e e^{\kappa} n \kappa^{-2n} \Gamma(2n) q / R(C_0, m) \quad (2)$$

where Γ is the gamma function, $q = b/a$ is the axial ratio of the Sérsic component, and $R(C_0, m)$ represents deviations from a perfect ellipse (Peng et al. 2010). This term has a value of the order of unity and is disregarded in our calculations.

Following Equation (4) in Terzić & Graham (2005) we have that the mass density of a Sérsic component is given by the

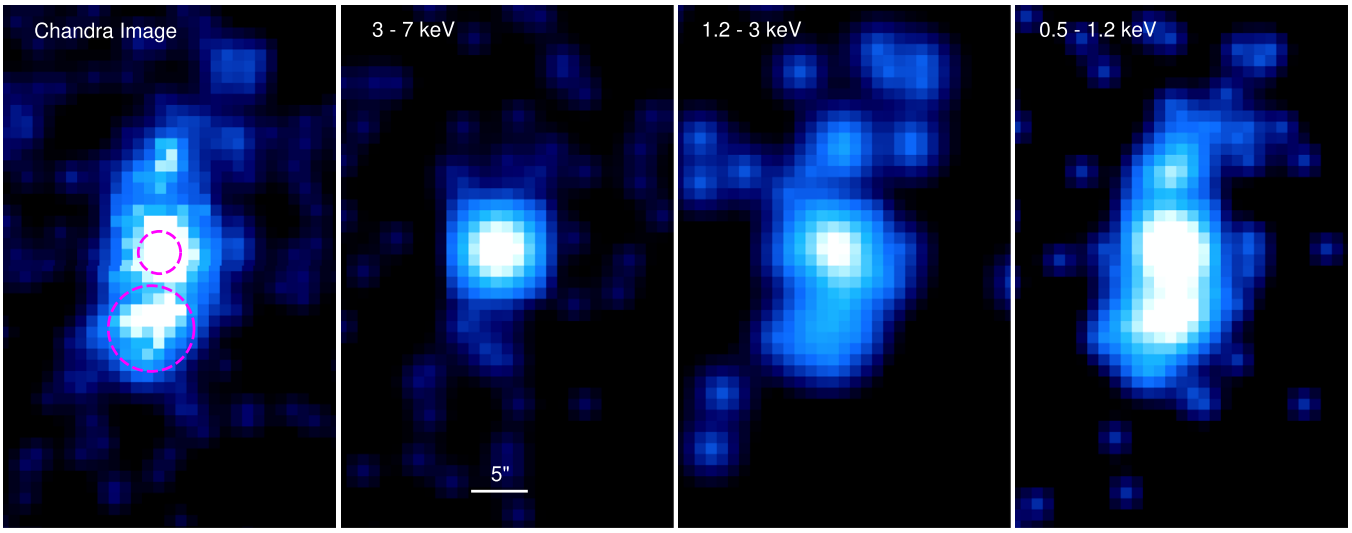

Figure 8. *Chandra* images of 2MASX J0423 in the full bandpass (left) and in the decomposed hard (left-center), medium (right-center), and soft (right) bandpasses. A 5″ scale bar is shown in the left-center panel; all images are on the same physical scale. The magenta dashed circles in the left panel denote the regions from which the spectra shown in Figure 9 were extracted. 5″ corresponds to a spatial scale of ∼4.5 kpc.

following expressions:

$$\rho(r) = \rho_0 \left(\frac{r}{r_e}\right)^{-p} e^{\kappa} e^{\left(-\kappa\left(\frac{r}{r_e}\right)^{1/n}\right)} \quad (3)$$

$$p = 1 - \frac{0.6097}{n} + \frac{0.05563}{n^2} \quad (4)$$

$$\rho_0 = \frac{M}{L} \Sigma_e \kappa^{n(1-p)} \frac{\Gamma(2n)}{2 r_e \Gamma(n(3-p))} \quad (5)$$

where M/L is the mass-to-light ratio, assumed to be 5 as in Terzić & Graham (2005). Notice that due to a difference in notation between Peng et al. (2010) and Terzić & Graham (2005), the expression for $\rho(r)$ has an additional e^{κ} term. Also, the expression for p corresponds to values of n in the range $0.6 < n < 10$.

Finally, we have from Equation (A2) in Terzić & Graham (2005) that the mass profile is given by

$$M(r) = 4\pi\rho_0 r_e^3 n \kappa^{n(p-3)} \gamma(n(3-p), Z) \quad (6)$$

where $\gamma(n(3-p), Z)$ is the incomplete gamma function and Z is given by $Z = \kappa(r/r_e)^{1/n}$. Using Equation (10) of Terzić & Graham (2005), we can calculate the enclosed mass at a given radius, as shown in Figure 16, and thus determine the gravitational deceleration at that radius.

In order to determine whether the emission-line gas can be radiatively accelerated in situ, we used the radiation–gravity formalism detailed in Das et al. (2007) and Fischer et al. (2017). If an azimuthally symmetric distribution is assumed, then $v(r)$, the velocity in units of km s^{-1} as a function of radial distance in parsecs, can be written as

$$v(r) = \sqrt{\int_{r_1}^{r} \left[6840 L_{44} \frac{\mathcal{M}}{r^2} - 8.6 \times 10^{-3} \frac{M(r)}{r^2}\right] dr}, \quad (7)$$

where L_{44} is the bolometric luminosity, $L_{\rm bol}$, in units of 10^{44} erg s^{-1}, $\mathcal{M}$ is the force multiplier, or the ratio of the total photoabsorption cross section to the Thomson cross section, $M(r)$ is the enclosed mass at the distance r, determined from the radial mass distribution described above, and r_1 is the launch radius of the gas. Calculating $M(r)$ required solving an incomplete Gamma function, hence we determined it at 10 pc intervals over a range 10 pc $< r <$ 10 kpc. We derived an expression for the enclosed mass as a function of r, in each 10 pc interval from r_1 to r_2, using a power law of the form $M(r) = M(r_1) \times (r_1/r_2)^{\beta}$. We were then able to solve for $v(r)$ analytically, by integrating within each interval, using an average β of 0.8.

We estimate the bolometric luminosity of the AGN in 2MASX J0423 using the intrinsic hard X-ray luminosity reported in Ricci et al. (2017) of $L_{2-10\,\rm keV} = 6.6 \times 10^{43}$ erg s^{-1} and a bolometric correction of 30 (Awaki et al. 2001), for a bolometric luminosity of $L_{\rm bol} = 2.0 \times 10^{45}$ erg s^{-1}. Additionally, we can estimate the bolometric luminosity from the integrated [O III] luminosity across the central SNIFS field, $L_{[\rm O\,III]} = 1.04 \times 10^{42}$ erg s^{-1}, and using a bolometric correction of 3500 (Heckman et al. 2004), for a similar bolometric luminosity of $L_{\rm bol} = 3.6 \times 10^{45}$ erg s^{-1}. Assuming that the AGN is radiating at the Eddington rate (i.e., $L_{\rm bol} = L_{\rm Edd}$), we can use the calculated bolometric luminosities for 2MASX J0423 to estimate a range in minimum SMBH masses of $M_{\rm BH} \geqslant (1.6\text{–}2.9) \times 10^7\,M_{\odot}$.

Photoionization models with log $U \approx -2$ to -2.5 predict that O^{+2} (i.e., [O III]) is the peak ionization state for oxygen (Ferland & Netzer 1983), and therefore it can be used to constrain the physical conditions in the [O III] emission-line gas. At this ionization, Cloudy predicts $\mathcal{M} = 3300$ at the ionized face of an illuminated slab, and we use this value to solve for $v(r)$.

Using our kinematic model to generate velocity distributions for knots of emission-line gas launched from various radii, we find that radiative driving should be successful throughout the inner 10 kpc of the system, which encompasses the entirety of the observed optical emission. However, while radiative driving may explain the kinematic offsets between emission lines throughout the system, the high FWHM gas and adjacent gas exhibiting large velocity offsets observed near the ends of the optical gas lanes cannot be produced by radiative driving at these distances. As such, an additional mechanism must contribute to the observed kinematics.

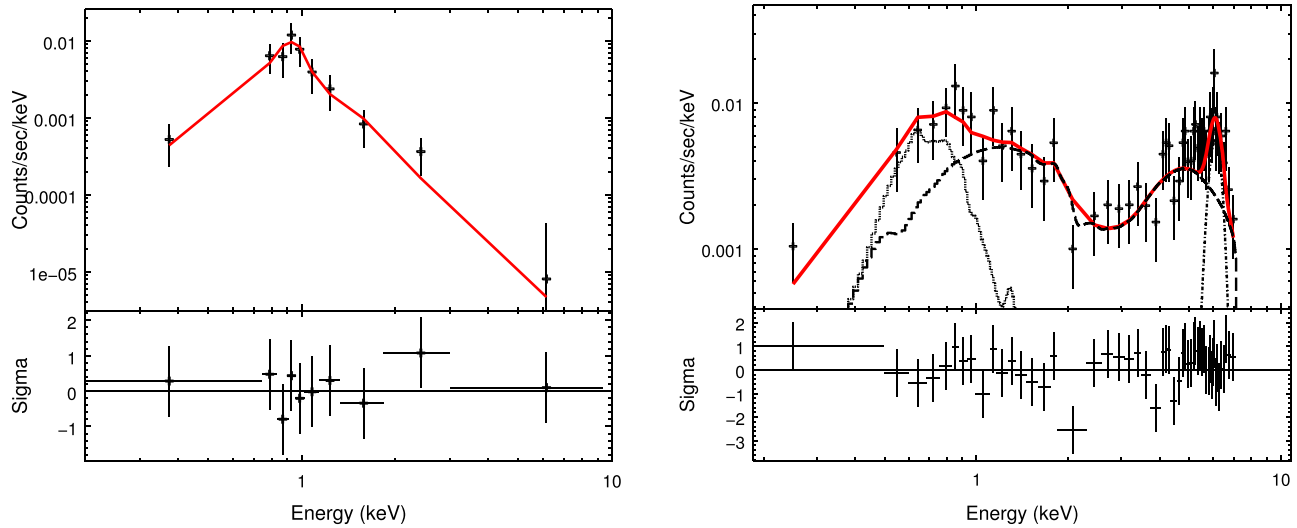

Figure 9. *Chandra* X-ray spectra and best-fitting models with residuals of the southern X-ray lobe (left) and the nucleus (right), extracted from the regions shown in Figure 8. The southern lobe model consists of only a thermal plasma model affected by Galactic absorption. The nucleus is best fit by a model consisting of a thermal plasma (dotted), an absorbed power law (dashed), and a Gaussian emission Fe Kα line (dotted–dashed).

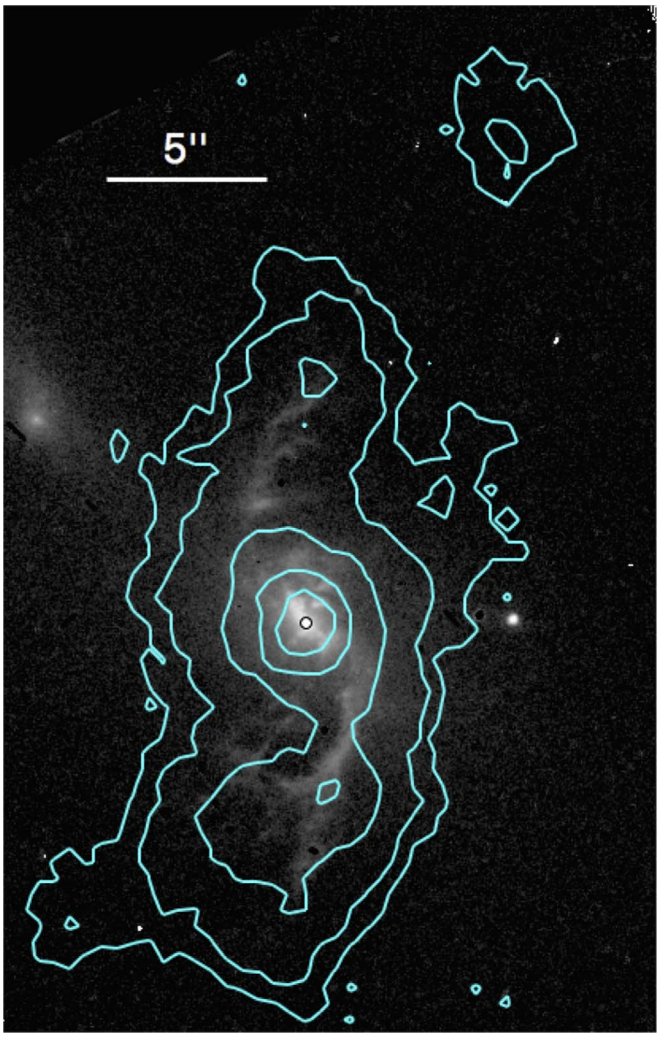

Figure 10. *HST* F675W imaging and full bandpass *Chandra* X-ray imaging (cyan contours) in 2MASX J0423. A black circle represents the optical emission peak and assumed nucleus position. 5″ corresponds to a spatial scale of ∼4.5 kpc.

4.3. Mechanically Driven Kinematics

One possibility that may explain the observed kinematics at large radii is that AGN winds driven from smaller radii are colliding with high-density gas lanes further out. As shown in Figure 17, continuous acceleration of optical clouds across the inner few hundred parsecs from the nucleus should result in knots of ionized gas traveling with velocities $v > 1000\,\mathrm{km\,s^{-1}}$, but such large velocities are not observed in this system. This may be due to the observed optical ionized gas outflows only tracing the surface of molecular gas reservoirs adjacent to the AGN ionizing radiation field. Unbound from the molecular gas reservoirs, outflows of optically emitting gas expand thermally and are further ionized into outflows of X-ray-emitting gas. Possessing a large filling factor, this X-ray wind is likely to be diffuse and difficult to detect until it comes into contact with high-density molecular gas lanes at larger radii. The X-ray winds then impart their energy into the gas lanes, which compress and shock the lane material, driving it laterally out of the plane of the disk, i.e., pancaking, producing the observed large velocity gradients, localized high FWHM kinematics, and LINER-like ionization diagnostics in regions near the ends of the observed gas lanes.

From our observations, the X-ray morphology across 2MASX J0423 also mimics the gas lane structures observed in our optical observations and is concentrated near the high FWHM kinematics observed in the optical. This suggests that the observed X-ray emission is likely continuum emission produced thermally via shocks. This is supported by our spectral energy distribution fit to the X-ray emission in the southern lobe, where we found the emission to best resemble a soft thermal plasma model with $kT = 0.97^{+0.106}_{-0.133}$ keV. Emission peaking at ≈1 keV is consistent with a shock velocity of approximately $1000\,\mathrm{km\,s^{-1}}$ (e.g., Kraemer & Crenshaw 2000) and the FWHM of the optical gas near the point of impact in the southern gas lane.

We model the constant energy injection rate going into the energy-conserving pancaked region following work by Nesvadba et al. (2006), assuming that the mechanically driven kinematics

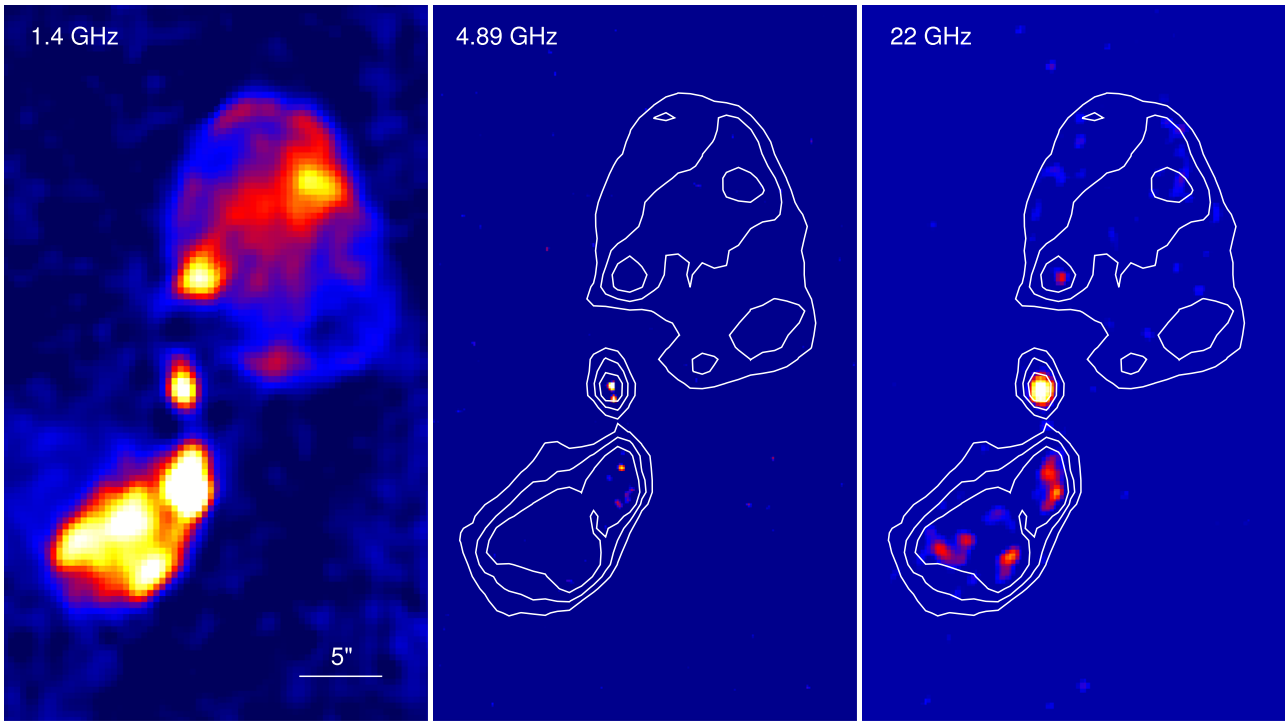

Figure 11. Left to right: VLA imaging of 1.45, 4.89, and 22 GHz emission in 2MASX J0423. Contours of 1.45 GHz are overlaid in the other bands for registration. North is up and east is to the left. 5″ corresponds to a spatial scale of ∼4.5 kpc.

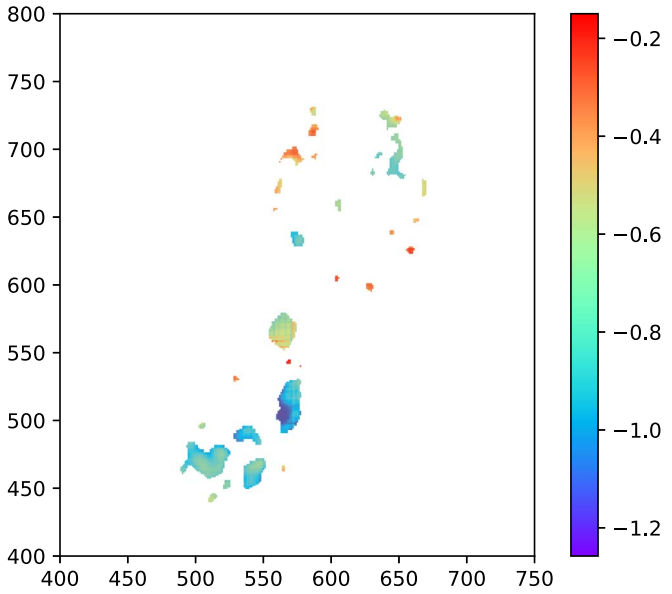

Figure 12. Spectral index map based on 3σ measurements from VLA 1.45 GHz and 22 GHz observations.

are expanding into a medium of low density, n_0. This provides a serviceable upper bound for an energy injection rate into the gas lane from the X-ray wind. Assuming minimal radiative losses, their Equation (3) defines a constant energy injection rate as

$$\dot{E} \approx 1.5 \times (\Omega/4\pi) \times 10^{46} R_{10}^2 v_{1000}^3 n_0 \text{ erg s}^{-1} \quad (8)$$

where the extent of the mechanically driven gas R_{10} is in units of 10 kpc, v_{1000} is in units of 1000 km s^{-1}, and $\Omega/4\pi$ is the covering factor of the driven gas in steradians. From the approximate measurement of FWHM $\sim$ 1000 km s^{-1} for the broad emission-line gas in the southern field of view, we measure a maximum outflow velocity defined as half the full width at zero maximum (FWZM), approximately the 3σ velocity offset from the centroid of the broad FWHM region, of $v = 1275$ km s^{-1}. Using $R_{10} = 2.4$, $v_{1000} = 1.275$, $\Omega/4\pi = 1.0$, and $n_0 = 0.5$, we calculate an energy injection rate of $\dot{E} = 8.95 \times 10^{44}$ erg s^{-1}. This is likely an upper limit because the covering factor and the density of the surrounding medium are likely overestimated.

Similar calculations for the X-ray wind impacting the northern gas lane produce an upper limit for the kinetic energy injection rate of $\dot{E} = 6.7 \times 10^{43}$ erg s^{-1}, using $R_{10} = 1.25$ kpc and $v_{1000} = 0.83$, derived by converting an average FWHM of the broader line region in the north of 650 km s^{-1} to a FWZM of 830 km s^{-1}, and $n_0 = 0.5$.

Interestingly, we also note that the brightest knots of radio emission are also colocated with the impact regions and resultant thermal X-ray emission in 2MASX J0423. For example, bifurcated radio knots surround the southern optical gas lane as shown in Figure 13, existing adjacent but laterally exterior to thermal X-ray emission and shocked, high FWHM optical emission. Following Zakamska & Greene (2014), this may be evidence that radio emission observed in this radio-quiet AGN is largely a by-product of relativistic particles accelerated in the shocks caused by the AGN-driven outflows. Although *HST* imaging does not trace gas lanes to larger radii, potentially thermal X-ray structures continue to trace the general path of the gas lanes, with cospatial, localized pockets of additional radio structure. This suggests that pressure from the X-ray winds colliding with gas lanes at larger radii continues to compress the molecular gas, forming shocks that in turn produce cosmic rays. The combination of cosmic rays

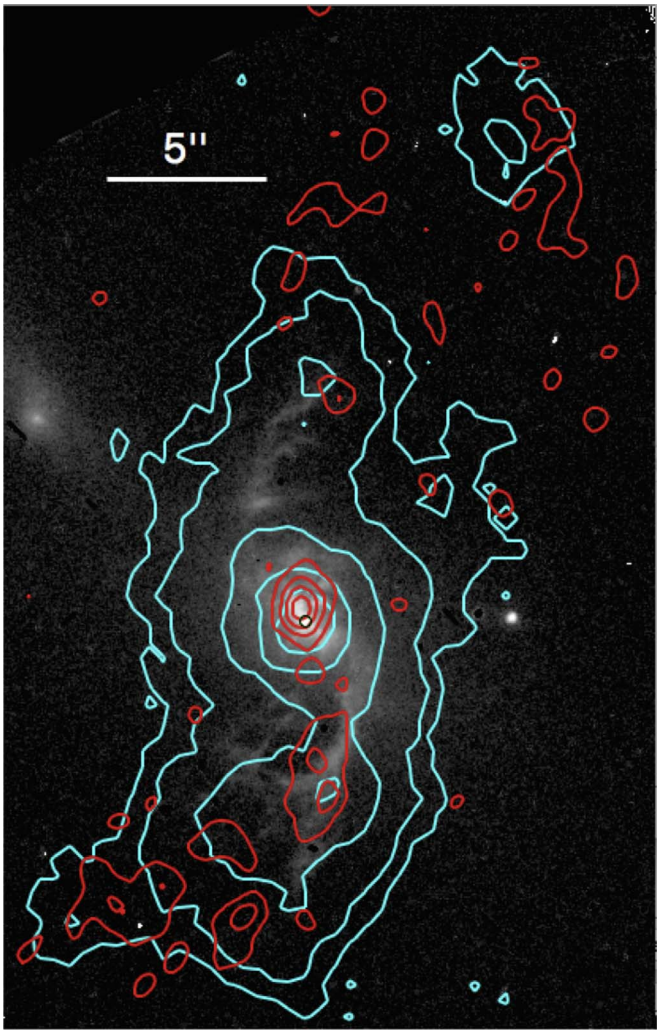

Figure 13. *HST* F675W imaging and full bandpass *Chandra* X-ray imaging and VLA 22 GHz emission as cyan and red contours, respectively, in 2MASX J0423. A black circle represents the optical emission peak and assumed nucleus position. 5″ corresponds to a spatial scale of ∼4.5 kpc.

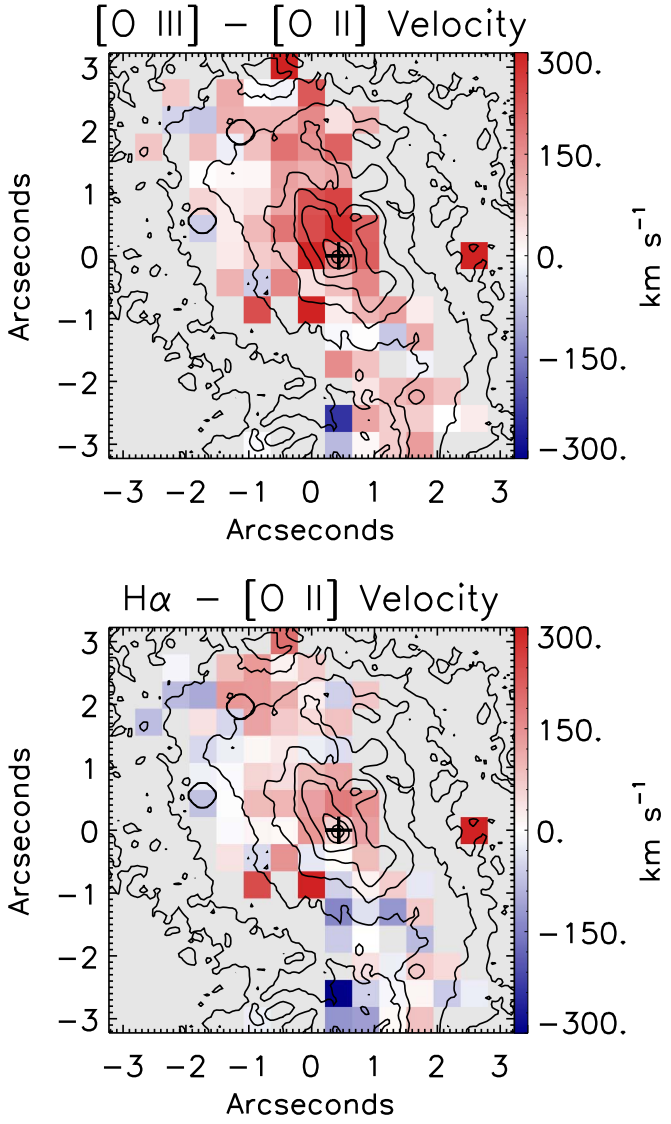

Figure 14. Velocity offsets between outflowing [O III] (top) and Hα (bottom) and rotating [O II] in the central SNIFS field of view. Velocity offsets are largest directly north of the nucleus. Black contours represent *HST*/WFPC2 F675W imaging.

and enhanced magnetic field lines in the compressed gas allows for the in situ formation of the observed radio structure, formation of the observed pseudo-jet morphology, and filling-up of the evacuated cavity at lower frequencies.

This production of radio emission is likely to be similar to processes in supernova remnants, where shocks initiated by the supernova wind accelerate particles and then produce synchrotron radiation (Zakamska & Greene 2014 and references therein). Therefore the efficiency of converting the kinetic energy of the outflow wind into radio synchrotron emission is assumed to be similar between quasar-driven and starburst-driven winds, where an efficiency of 3.6×10^{-5} is required to convert kinetic energy into 1.4 GHz radio luminosity.

From the archival VLA 1.4 GHz observations, we measure fluxes of the radio knots adjacent to the high FWHM optical regions north and south of the AGN and calculate luminosities of $\nu L_\nu(1.425\,\mathrm{GHz}) = 2.65 \times 10^{39}\,\mathrm{erg\,s^{-1}}$ and $2.94 \times 10^{40}\,\mathrm{erg\,s^{-1}}$, respectively. Comparing these values to the calculated energy injection rates required to produce the laterally expanding optical kinematics described above, we measure efficiencies of 3.95×10^{-5} and 3.28×10^{-5} for the north and south regions, respectively, which are consistent with that required to produce synchrotron emission via starburst-driven winds.

The differences in flux and FWHM in the north and south gas lanes are likely due to the interaction between AGN radiation and host disk material immediately north of the AGN

Table 1
GALFIT Model Results

Component	I (mag)	r_e (kpc)	n	b/a	PA (deg)
1	15.78	3.34	4.44	0.71	36.73
2	15.79	9.48	0.75	0.48	67.27
3	19.78	0.57	0.83	0.48	100.63

Note. Column (1) is the Sérsic component, column (2) is integrated *I*-band magnitude, column (3) is effective radius, column (4) is Sérsic index, column (5) is axial ratio, and column (6) is position angle east of north.

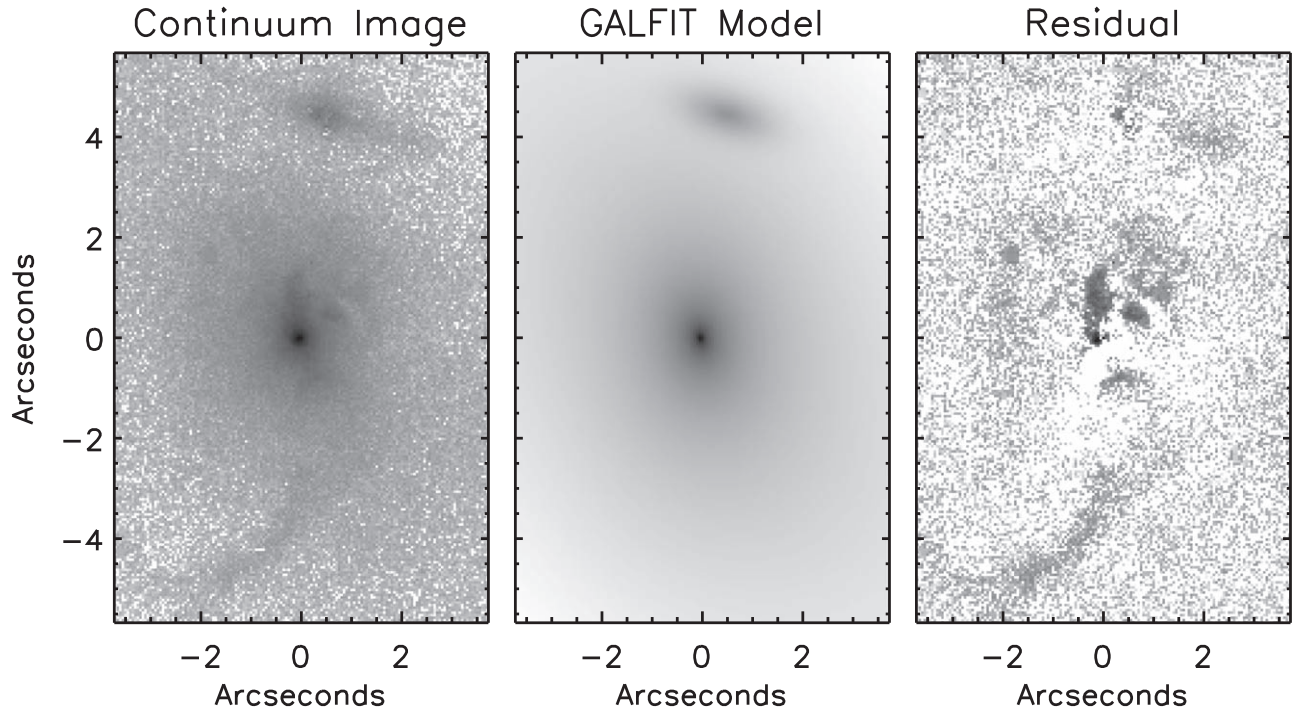

Figure 15. Left: *HST* WFPC2/PC F814W continuum image of 2MASX J0423. Center: best-fit galaxy decomposition model (two components + background galaxy) for 2MASX J0423. Right: residuals between image and model.

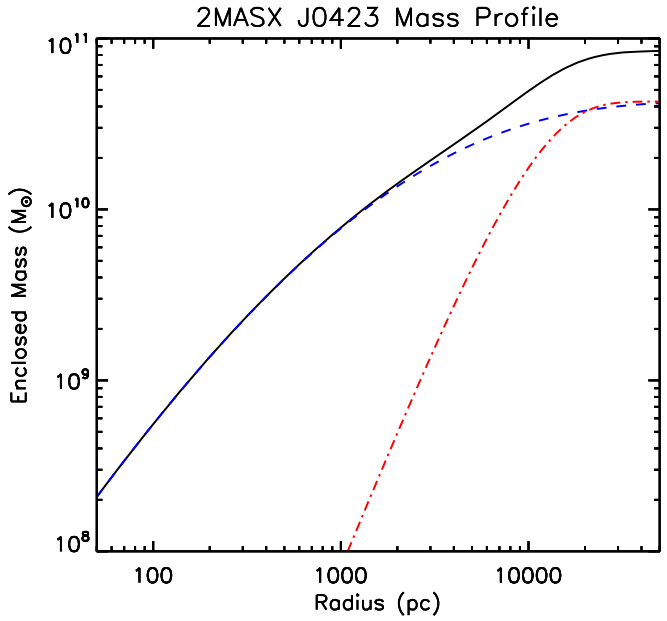

Figure 16. Mass distribution profiles for each component of 2MASX J0423 in our model. Blue dashed, red dotted–dashed, and black solid lines represent the inner and outer components, and the sum of the two components, respectively. Our radial mass distribution is calculated using the expressions from Terzić & Graham (2005) assuming a mass-to-light ratio of 5.

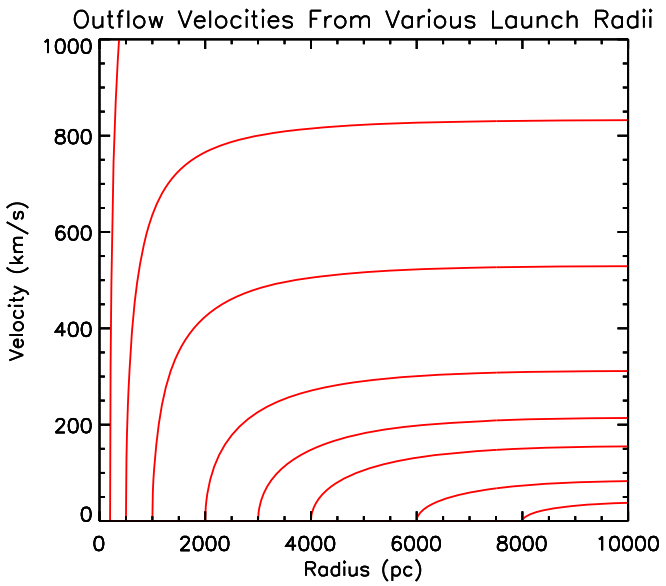

Figure 17. Velocity profiles for knots of [O III] gas in 2MASX J0423 launched from various radii (all generated assuming $\mathcal{M} = 3300$), in the absence of interaction with an ambient medium. Based on these results, radiatively accelerated gas can be driven throughout the inner 10 kpc.

nucleus where the largest velocity offsets in Figure 14 are observed. Here, we see large concentrations of optical, X-ray, and radio emission, which suggests that the mechanical processes observed at large radii are also occurring here. However, as the impact of the wind onto the host gas lane is likely at a more oblique angle than the impacts observed at larger radii, it is difficult to derive observed optical energy injection rates to test the relationship between injected energy and observed 1.4 GHz radio luminosity.

5. Discussion

From our analysis, we attribute the observed optical kinematics to three distinct distributions.

(1) A general rotation pattern, more easily observed in emission lines of lower ionization potential (i.e., [O II]). The northern lane is redshifted, rotating into the plane of

the sky, and the southern lane is blueshifted, rotating out of the plane of the sky.

(2) Radially outflowing kinematics traveling away from the nuclear continuum peak via radiative driving, observed as velocity differences between emission lines with different ionization potentials. Velocities for [O III] are redshifted compared to other emission lines both north and south of the AGN nucleus.

(3) Laterally outflowing kinematics approximately perpendicular to the radial outflows via mechanical driving at radial distances greater than 5″, observed both as velocity gradients across lane structures and as high FWHM emission lines. The largest gradients in both the north and south fields are radially colocated with high FWHM gas regions at the end of the optical gas lane structures, which suggests that the velocity shifts are the expanding edges of the high FWHM region.

With continuous outflows traveling radially outward potentially through the entire observed optical system, 2MASX J0423 has outflows of radiatively driven optical ionized gas, defined as radial velocities offset from systemic, larger than those observed in a majority of nearby Type 2 AGNs in spatially resolved kinematic studies, which typically exhibit maximum outflow distances of 1–2 kpc (Fischer et al. 2013, 2018). Our measurements suggest that the bolometric luminosity of this system is not exceptional. However, the relatively small stellar mass within the host for this system allows outflows to exist throughout the system, assuming an absence of interactions with the ambient medium (i.e., lanes of high-density molecular gas). As such, we suggest that the mass ratio between the stellar bulge of a galaxy and its SMBH is critical in determining whether feedback works. Extending this to systems near Cosmic Noon, where bulges were typically defined, AGNs are likely to be more successful in the smaller gravitational potentials of their host galaxies.

Our analysis also suggests that the extent of optical, radially driven, high-velocity outflows does not define the maximum radius of impact for AGN feedback in a host galaxy. In previous high-resolution studies of [O III] kinematics in luminous QSO2s (Fischer et al. 2018), ionized gas kinematics exhibited high-velocity radial outflows at small radii, and returned to systemic velocity or followed a rotation pattern at larger radii. However, this gas at large radii is likely experiencing some influence by the AGN because kinematics at these distances often exhibited large FWHM values indicative of some kinematic disturbance (Bellocchi et al. 2013; Ramos Almeida et al. 2017). If these targets follow a similar scenario to 2MASX J0423, the optical ionized, radially outflowing gas at small radii in these systems is likely further ionized to become an X-ray wind, which continues out to greater distances than what is observed via optical and near-infrared measurements and impacts the previously rotating, photoionized host disk gas. It is currently extremely difficult to obtain spatially resolved X-ray spectroscopy and measure the kinematics of the diffuse outflows in the X-ray, so we can instead use signatures of the wind disrupting ambient host material, in the form of large FWHM optical and infrared emission lines, and by-products of thermal X-ray emission, and extended synchotron radio emission, to act as a proxy for the extent of outflowing AGN winds interacting with their hosts in radio-quiet AGNs.

It is notable that when radio structures are well aligned with optical ionized gas structures, they must be approximately aligned with high-density gas lanes in the system, because the optical structures have been shown to be the ionized surfaces of molecular gas reservoirs (i.e., gas lanes; Fischer et al. 2017). If the observed radio emission was from a radio jet, then to strongly interact with the southern gas lane of 2MASX J0423, as observed at a distance of ≈4.65 kpc from the nucleus, and assuming a lane scale height of 500 pc, it would need to be aligned within 3° of the lanes. Given a random alignment between jet axis and plane, the probability of successful alignment within 3° is ∼5%. Previous analysis of radio and optical alignment (Falcke et al. 1998; Kukula et al. 1999) shows that extended radio emission is often intertwined or aligned with the optical structure in a similar fashion to 2MASX J0423. As such, having radio emission and adjacent gas ionization and non-rotating kinematics be due to a radio jet would require the axis of the jets observed in these targets to consistently be almost perfectly aligned with the plane of the disk or gas lanes.

We find that several targets share similarities to 2MASX J0423, including SDSS J1356+1026, a merging system housing a Type 2 AGN at $z = 0.123$. Optical spectroscopy for the system largely consists of emission from the two nuclei and a kinematic "bubble" that produces a ring-like [O III] structure in the two-dimensional spectrum, extending 8–12 kpc from the AGN nucleus, and exhibits velocities $\sim\pm230\,\mathrm{km\,s^{-1}}$ from systemic (Greene et al. 2012). These kinematics are attributed to a shell of gas expanding into the intergalactic medium, similar to the mechanical driving that we observe in the optical kinematics of the southern gas lane of 2MASX J0423, where [O III] gas is fainter near the X-ray impact point and brighter in the expanding mechanically driven gas. Additionally, *Chandra* X-ray observations show similar relationships between extended structures in the optical and soft X-ray (Greene et al. 2014; Comerford et al. 2015), such that the bright optical bubble feature is colocated with the brightest extended X-ray emission. These similarities suggest that the kinematics at multi-kiloparsec distances in SDSS J1356+1026 are likely due to shocked gas associated with AGN-driven outflows. High-resolution, high-sensitivity VLA radio continuum observations do not yet exist for this target; however, detecting extended radio emission intertwined with the extended X-ray and optical structure would confirm that similar processes to those in 2MASX J0423 are in play.

Another target with striking similarities to 2MASX J0423 that does have optical, X-ray, and radio imaging is NGC 4258—a Seyfert galaxy believed to possess large radio jets driven by the AGN that lie within the plane of the star-forming spiral host galaxy and have therefore interacted strongly with the interstellar medium (van der Kruit et al. 1972). The radio structures have been referred to as "anomalous arms," and several studies of this source discuss the jet–gas interaction, how matter in the host galaxy can be entrained, heated, or shocked by the jet, and how the galaxy's spiral stellar structure responds to such a disruption (e.g., Martin et al. 1989; Cecil et al. 2000; Laine et al. 2010). Imaging of this target exhibits two prominent arms north and south of the nucleus in the optical, which spiral outward and are dominated by young, bright stars, with the anomalous arms visible in Hα, soft X-ray, and radio continuum (Cecil et al. 1992; Yang et al. 2007). Spatially resolved X-ray spectroscopy reveals the extended soft

X-ray emission for the entire galaxy to be well described by thermal components, suggesting that the gas is heated by shocks traveling at velocities similar to those implied by optical kinematic measurements. Figure 7(b) in Cecil et al. (1995) orients the radio structure to a position that is remarkably similar to 2MASX J0423 and exhibits a very similar radio morphology—a bright radio structure immediately above the nucleus with a fainter structure at large radii and a bright radio structure below the nucleus at large radii, with large FWHMs present in Hα when not extinguished by the host disk. The northwest radio arm in NGC 4258 is also bifurcated, similar to the south radio arm of 2MASX J0423. We found the radio structure to separate around the optical gas lane structure, beginning near the X-ray impact region that exhibits high FWHM optical lines. Assuming a similar scenario in NGC 4258, forking in the northwest lane of NGC 4258 also begins near an apparent X-ray impact region that exhibits high FWHM optical lines, which suggests that the AGN feedback processes in NGC 4258 may also be related to winds.

Findings from 2MASX J0423 also provide further understanding in our previous kinematic analysis of Mrk 573 in Fischer et al. (2017), where we initially decoded non-rotating ionized gas kinematics along the axis of the projected NLR as radiative, in situ acceleration of material residing in the host disk. At the furthest extents of non-rotating gas, however, there are also co-radial knots of ionized gas that continue to follow rotation as measured by stellar kinematics. Applying the kinematic explanation we derive for 2MASX J0423, the non-rotating kinematics at distances >500 pc are likely the by-product of winds launched from smaller radii. These winds run into dust lanes, shocking the dense medium, forming in situ X-ray and radio emission, and creating the same pancaking optical kinematic profile we observe in 2MASX J0423, which disturbs the intrinsic, rotating ENLR gas. This scenario is supported through several observations across similar wavebands to those in this analysis. *HST* [O III] long-slit spectroscopy of the arcs in Mrk 573 from Fischer et al. (2010) exhibits velocity gradients across each of the three arcs illuminated by the AGN, similar to the gradients we see in 2MASX J0423. *Chandra* X-ray flux distributions in Paggi et al. (2012) are aligned such that photoionized line emission traces the linear, optical outflowing region and the interior side of the optical arcs. Radio structures are also aligned with the optical gas, where high-resolution 8.49 GHz observations show emission located along the linear feature that has the largest adjacent H_2 reservoir (i.e., densest spiral arm) and in between the linear outflows and pancaking arcs (Falcke et al. 1998). Lower resolution 5 GHz emission forms a reservoir interior to the arcs, filling the area between the outflows and gas lane arcs (Paggi et al. 2012). Ionized gas kinematics in several other AGNs (e.g., Mrk 34, NGC 3516, NGC 3393; Fischer et al. 2013) also exhibit velocity gradients centered on the rotational velocity kinematics at large radii that are likely similar examples of X-ray winds pancaking into molecular gas lanes.

6. Conclusions

We analyzed SNIFS optical IFU spectroscopy and imaging from *HST*, *Chandra*, and VLA observatories to measure optical ionized gas kinematics and ionization sources, X-ray spectral diagnostics, radio spectral indices, and the morphological relationship between the three wavebands. Our conclusions are as follows.

(1) Radiative driving of optical, AGN-ionized gas is possible throughout the inner 10 kpc of this system, encompassing the entirety of the observed optical emission. Successful driving of [O III] gas out to multi-kiloparsec scales in this system is due to a less concentrated mass profile in the host galaxy than in other AGN of similar luminosity. As more luminous AGNs with more massive hosts exhibit less productive radial outflow, we suggest that lower host masses may be critical for galaxies to regularly quench star formation.
(2) Optical high FWHM gas near systemic velocity or following rotational patterns observed at large radii in this system cannot be produced by radiative driving and therefore does not trace the maximum extent at which optical gas can be driven by the AGN. Instead, such a signature likely measures the extent of outflows of X-ray-emitting gas, launched from smaller radii, driving into high-density gas lanes at large radii and laterally pushing the ambient lane gas.
(3) Outflows driving into these dense lanes also produce shocks that heat and compress the lane gas, producing a significant amounts of thermal X-rays and cosmic rays, which in turn allow for the in situ formation of radio knots. Therefore observed extended soft X-ray and radio continuum emission in this target, and likely other radio-quiet AGNs, may often be by-products of radiatively driven winds originating at smaller radii.

The authors thank the anonymous referee for their helpful comments that improved the clarity of this work.

T.C.F. thanks Mitchell Revalski, Beena Meena, Francisco Martinez, and Garrett Polack for insightful discussions, and Nathan Secrest for guidance in astrometric alignment between images.

K.L.S. is grateful for support from the National Aeronautics and Space Administration through Einstein Postdoctoral Fellowship Award Number PF7-180168, issued by the *Chandra* X-ray Observatory Center, which is operated by the Smithsonian Astrophysical Observatory for and on behalf of the National Aeronautics and Space Administration under contract NAS8-03060.

Based on observations made with the NASA/ESA *Hubble Space Telescope*, obtained from the data archive at the Space Telescope Science Institute. STScI is operated by the Association of Universities for Research in Astronomy, Inc. under NASA contract NAS 5-26555. Support for this work was provided by NASA through the Space Telescope Science Institute, which is operated by AURA, Inc., under NASA contract NAS 5-26555.

The scientific results reported in this article are based in part on observations made by the *Chandra* X-ray Observatory.

The National Radio Astronomy Observatory is a facility of the National Science Foundation operated under cooperative agreement by Associated Universities, Inc.

Appendix
Additional Optical Emission Line Measurements with SNIFS

Additional optical emission line measurements with SNIFS are shown in Figure 18 for [O I] λ6300, in Figure 19 for [S II] λ6716, and in Figure 20 for [Ne III] λ3869, Hβ, and [S III] λ9071 lines.

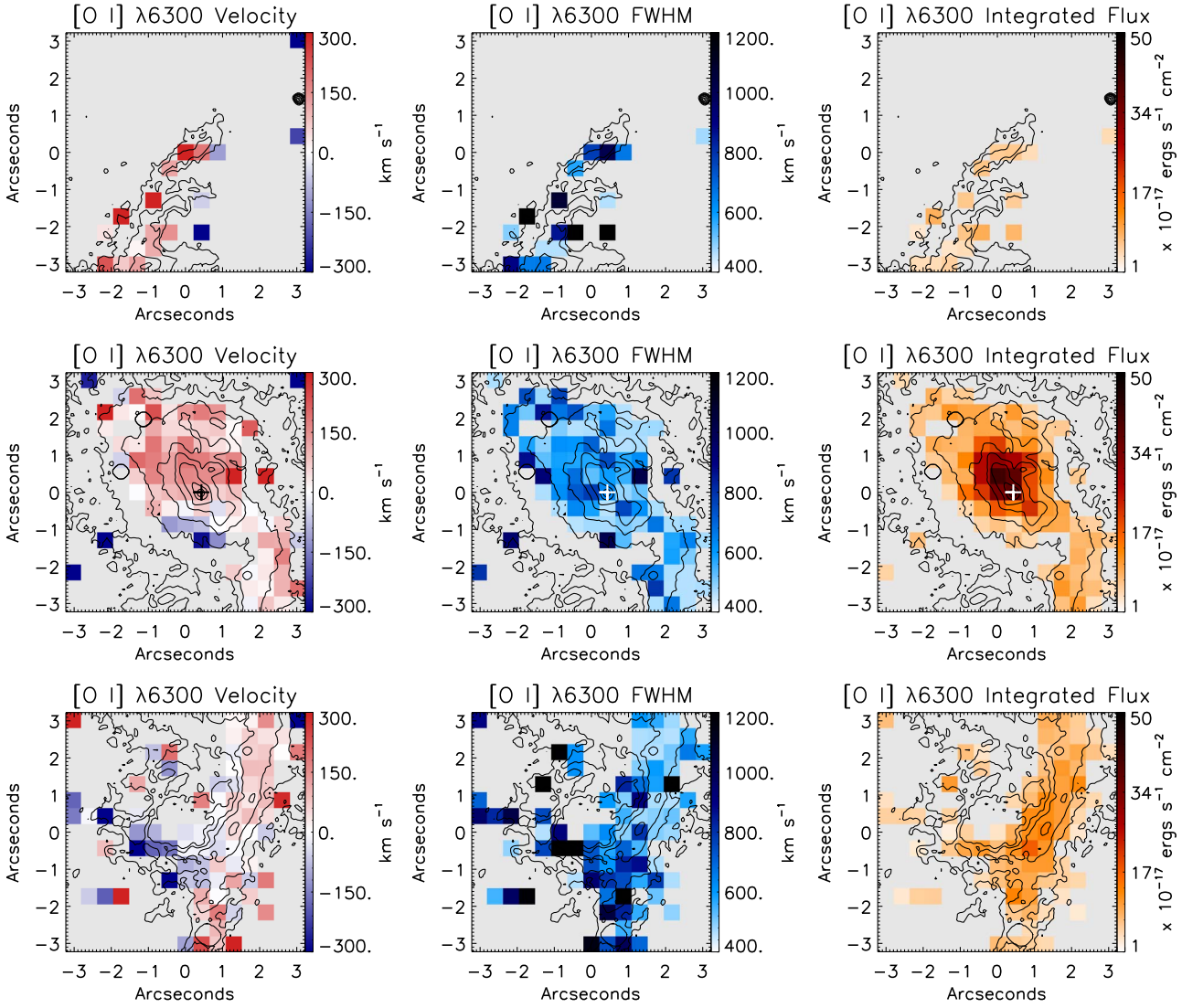

Figure 18. [O I] λ6300 kinematic measurements in 2MASX J0423 from SNIFS IFU observations. First, second, and third columns display emission-line profile centroid velocity, FWHM, and integrated flux maps, respectively. First, second, and third rows display measurements for the top, center, and bottom fields of view, respectively. Black contours represent *HST*/WFPC2 F675W imaging. The optical continuum flux peak is depicted by a cross. One $0\farcs4 \times 0\farcs43$ spaxel samples approximately 380 pc $\times$ 380 pc.

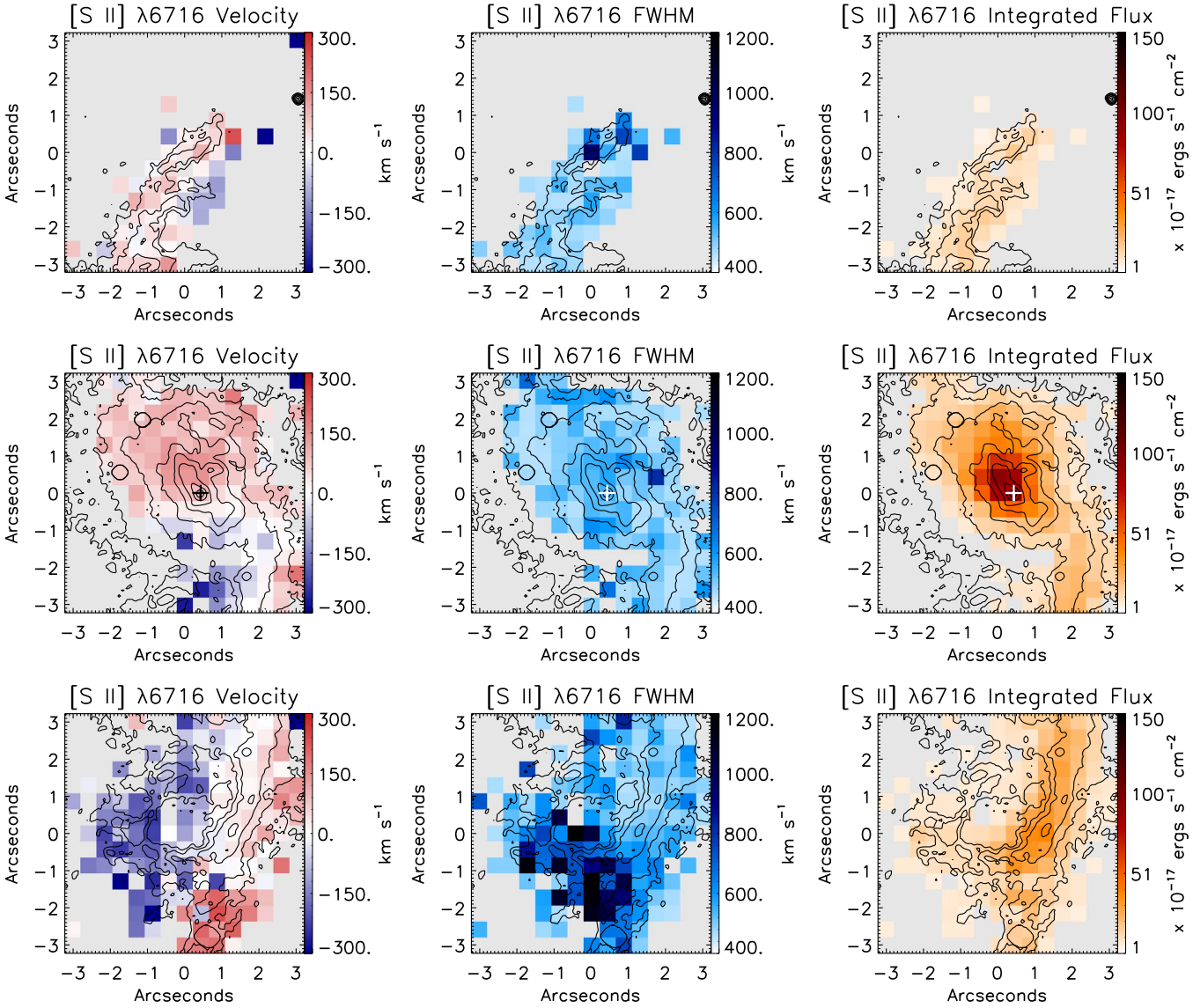

Figure 19. [S II] λ6716 kinematic measurements in 2MASX J0423 from SNIFS IFU observations. First, second, and third columns display emission-line profile centroid velocity, FWHM, and integrated flux maps, respectively. First, second, and third rows display measurements for the top, center, and bottom fields of view, respectively. Black contours represent *HST*/WFPC2 F675W imaging. The optical continuum flux peak is depicted by a cross. One $0\farcs4 \times 0\farcs43$ spaxel samples approximately 380 pc $\times$ 380 pc.

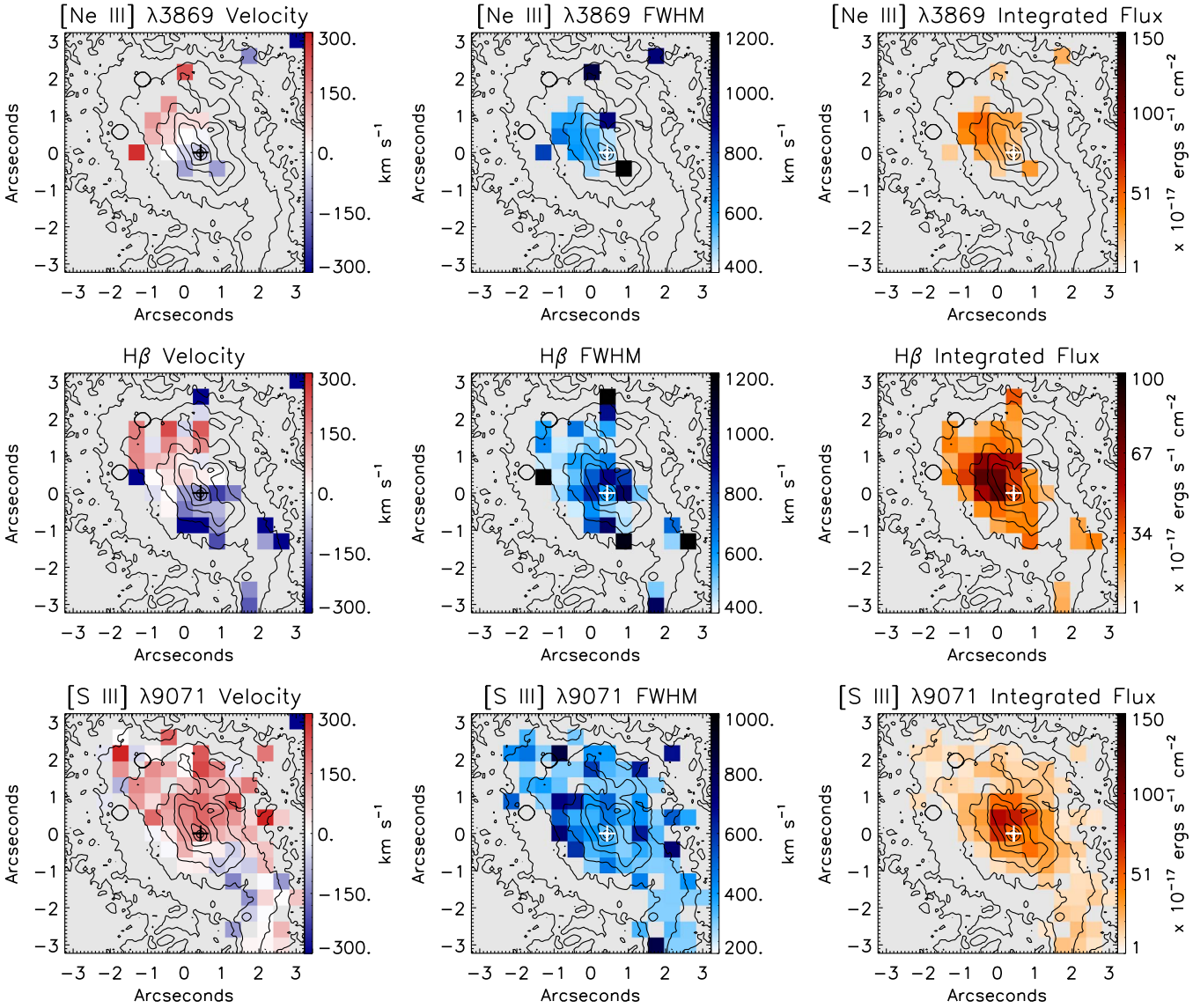

Figure 20. Nuclear [Ne III] λ3869 (top row), Hβ (middle row), and [S III] λ9071 (bottom row) kinematic measurements in 2MASX J0423 from SNIFS IFU observations in the central field of view. First, second, and third columns display emission-line profile centroid velocity, FWHM, and integrated flux maps, respectively. Black contours represent *HST*/WFPC2 F675W imaging. The optical continuum flux peak is depicted by a cross. One $0\farcs4 \times 0\farcs43$ spaxel samples approximately 380 pc $\times$ 380 pc.

ORCID iDs

Krista Lynne Smith https://orcid.org/0000-0001-5785-7038
Henrique Schmitt https://orcid.org/0000-0001-7376-8481
Michael Koss https://orcid.org/0000-0002-7998-9581
Richard Mushotzky https://orcid.org/0000-0002-7962-5446
Kirsten Larson https://orcid.org/0000-0003-3917-6460
Vivian U https://orcid.org/0000-0002-1912-0024
Jane Rigby https://orcid.org/0000-0002-7627-6551

References

Aldering, G., Adam, G., Antilogus, P., et al. 2002, Proc. SPIE, 4836, 61
Aldering, G., Antilogus, P., Bailey, S., et al. 2006, ApJ, 650, 510
Awaki, H., Terashima, Y., Hayashida, K., & Sakano, M. 2001, PASJ, 53, 647
Bacon, R., Copin, Y., Monnet, G., et al. 2001, MNRAS, 326, 23
Baldwin, J. A., Phillips, M. M., & Terlevich, R. 1981, PASP, 93, 5
Begelman, M. C. 2004, in Coevolution of Black Holes and Galaxies, ed. L. C. Ho (Cambridge: Cambridge Univ. Press), 374
Beichman, C., Wynn-Williams, C. G., Lonsdale, C. J., et al. 1985, ApJ, 293, 148
Bellocchi, E., Arribas, S., Colina, L., & Miralles-Caballero, D. 2013, A&A, 557, A59
Buchner, J., Georgakakis, A., Nandra, K., et al. 2014, A&A, 564, A125
Cattaneo, A., Faber, S. M., Binney, J., et al. 2009, Natur, 460, 213
Cecil, G., Greenhill, L. J., DePree, C. G., et al. 2000, ApJ, 536, 675
Cecil, G., Wilson, A. S., & Tully, R. B. 1992, ApJ, 390, 365
Cecil, G., Wilson, A. S., & de Pree, C. 1995, ApJ, 440, 181
Comerford, J. M., Pooley, D., Barrows, R. S., et al. 2015, ApJ, 806, 219
Das, V., Crenshaw, D. M., & Kraemer, S. B. 2007, ApJ, 656, 699
Di Matteo, T., Springel, V., & Hernquist, L. 2005, Natur, 433, 604
Ellison, S. L., Teimoorinia, H., Rosario, D. J., & Mendel, J. T. 2016, MNRAS, 458, L34
Falcke, H., Wilson, A. S., & Simpson, C. 1998, ApJ, 502, 199
Ferland, G. J., & Netzer, H. 1983, ApJ, 264, 105
Feroz, F., & Hobson, M. P. 2008, MNRAS, 384, 449
Feroz, F., Hobson, M. P., & Bridges, M. 2009, MNRAS, 398, 1601
Feroz, F., Hobson, M. P., Cameron, E., & Pettitt, A. N. 2013, arXiv:1306.2144
Ferrarese, L., & Merritt, D. 2000, ApJL, 539, L9
Fischer, T. C., Crenshaw, D. M., Kraemer, S. B., & Schmitt, H. R. 2013, ApJS, 209, 1
Fischer, T. C., Crenshaw, D. M., Kraemer, S. B., Schmitt, H. R., & Trippe, M. L. 2010, AJ, 140, 577
Fischer, T. C., Machuca, C., Diniz, M. R., et al. 2017, ApJ, 834, 30

Fischer, T. C., Krarmer, S. B., Schmitt, H. R., et al. 2018, ApJ, 856, 102
Fruscione, A., McDowell, J. C., Allen, G. E., et al. 2006, Proc. SPIE, 6270, 62701V
Gebhardt, K., Kormendy, J., Ho, L. C., et al. 2000, ApJL, 543, L5
Greene, J. E., Pooley, D., Zakamska, N. L., Comerford, J. M., & Sun, A.-L. 2014, ApJ, 788, 54
Greene, J. E., Zakamska, N. L., & Smith, P. S. 2012, ApJ, 746, 86
Gültekin, K., Richstone, D. O., Gebhardt, K., et al. 2009, ApJ, 698, 198
Heckman, T. M., Kauffmann, G., Brinchmann, J., et al. 2004, ApJ, 613, 109
Hill, G. J., Wynn-Williams, C. G., Becklin, E. E., & MacKenty, J. W. 1988, ApJ, 335, 93
Holloway, A. J., Steffen, W., Pedlar, A., et al. 1996, MNRAS, 279, 171
Hopkins, A. M., & Beacom, J. F. 2006, ApJ, 651, 142
Hopkins, P. F., Cox, T. J., Kereš, D., & Hernquist, L. 2008, ApJS, 175, 390
Klamer, I. J., Ekers, R. D., Sadler, E. M., & Hunstead, R. W. 2004, ApJL, 612, L97
Koss, M., Mushotzky, R., Treister, E., et al. 2012, ApJL, 746, L22
Koss, M., Mushotzky, R., Veilleux, S., et al. 2011, ApJ, 739, 57
Koss, M., Trakhtenbrot, B., Ricci, C., et al. 2017, ApJ, 850, 74
Kraemer, S. B., & Crenshaw, D. M. 2000, ApJ, 544, 763
Kukula, M. J., Ghosh, T., Pedlar, A., & Schilizzi, R. T. 1999, ApJ, 518, 117
Laine, S., Krause, M., Tabatabaei, F. S., & Siopis, C. 2010, AJ, 140, 1084
Lantz, B., Aldering, G., Antilogus, P., et al. 2004, Proc. SPIE, 5249, 146
Martin, P., Roy, J.-R., Noreau, L., & Lo, K. Y. 1989, ApJ, 345, 707
McMullin, J. P., Waters, B., Schiebel, D., Young, W., & Golap, K. 2007, in ASP Conf. Ser. 376, Astronomical Data Analysis Software and Systems XVI, ed. R. A. Shaw, F. Hill, & D. J. Bell (San Francisco, CA: ASP), 127
Müller-Sánchez, F., Hicks, E. K. S., Malkan, M., et al. 2018, ApJ, 858, 48
Nandra, K., O'Neill, P. M., George, I. M., & Reeves, J. N. 2007, MNRAS, 382, 194
Nesvadba, N. P. H., Lehnert, M. D., Eisenhauer, F., et al. 2006, ApJ, 650, 693
Neumann, J., Gadotti, D. A., Wisotzki, L., et al. 2019, A&A, 627, A26
Paggi, A., Wang, J., Fabbiano, G., Elvis, M., & Karovska, M. 2012, ApJ, 756, 39
Peng, C. Y., Ho, L. C., Impey, C. D., & Rix, H.-W. 2002, AJ, 124, 266
Peng, C. Y., Ho, L. C., Impey, C. D., & Rix, H.-W. 2010, AJ, 139, 2097
Peterson, B. M. 1997, An Introduction to Active Galactic Nuclei (Cambridge: Cambridge Univ. Press)
Ramos Almeida, C., Piqueras López, J., Villar-Martín, M., & Bessiere, P. S. 2017, MNRAS, 470, 964
Ricci, C., Trakhtenbrot, B., Koss, M. J., et al. 2017, Natur, 549, 488
Riffel, R. A., Storchi-Bergmann, T., Riffel, R., et al. 2018, MNRAS, 474, 1373
Salim, S., Rich, R.M., Charlot, S., et al. 2007, ApJS, 173, 267
Schawinski, K., Lintott, C. J., Thomas, D., et al. 2009, ApJ, 690, 1672
Shimizu, T. T., Mushotzky, R. F., Meléndez, M., Koss, M., & Rosario, D. J. 2015, MNRAS, 452, 1841
Smith, K. L., Mushotzky, R. F., Vogel, S., Shimizu, T. T., & Miller, N. 2016, ApJ, 832, 163
Springob, C. M., Haynes, M. P., Giovanelli, R., & Kent, B. R. 2005, ApJS, 160, 149
Steffen, W., Holloway, A. J., & Pedlar, A. 1996, MNRAS, 282, 130
Terzić, B., & Graham, A. W. 2005, MNRAS, 362, 197
Turner, T. J., George, I. M., Nandra, K., & Mushotzky, R. F. 1997, ApJS, 113, 23
van der Kruit, P. C., Oort, J. H., & Mathewson, D. S. 1972, A&A, 21, 169
van Dokkum, P. G. 2001, PASP, 113, 1420
Wright, E. L. 2006, PASP, 118, 1711
Yang, Y., Li, B., Wilson, A. S., & Reynolds, C. S. 2007, ApJ, 660, 1106
Zakamska, N. L., & Greene, J. E. 2014, MNRAS, 442, 784